Journal of Magnetic Resonance **154,** 101–129 (2002)
doi:10.1006/jmre.2001.2464, available online at http://www.idealibrary.com on IDEAL®

Rotor-Encoded Heteronuclear MQ MAS NMR Spectroscopy of Half-Integer Quadrupolar and Spin $I = 1/2$ Nuclei[1]

Adonis Lupulescu,[2] Steven P. Brown,[3] and Hans Wolfgang Spiess[4]

Max-Planck-Institut für Polymerforschung, Postfach 3148, D-55021 Mainz, Germany

Received July 12, 2001; revised October 19, 2001

A new two-dimensional heteronuclear multiple-quantum magic-angle spinning (MQ MAS) experiment is presented which combines high resolution for the half-integer quadrupolar nucleus with information about the dipolar coupling between the quadrupolar nucleus and a spin $I = 1/2$ nucleus. Homonuclear MQ coherence is initially created for the half-integer quadrupolar nucleus by a single pulse as in a standard MQ MAS experiment. REDOR recoupling of the heteronuclear dipolar coupling then allows the creation of a heteronuclear multiple-quantum coherence comprising multiple- and single-quantum coherence of the quadrupolar and spin $I = 1/2$ nucleus, respectively, which evolves during t_1. Provided that the t_1 increment is not rotor synchronized, rotor-encoded spinning-sideband patterns are observed in the indirect dimension. Simulated spectra for an isolated IS spin pair show that these patterns depend on the recoupling time, the magnitude of the dipolar coupling, the quadrupolar parameters, as well as the relative orientation of the quadrupolar and dipolar principal axes systems. Spectra are presented for Na_2HPO_4, with the heteronuclear ^{23}Na–^1H MQ MAS experiments beginning with the excitation of ^{23}Na (spin $I = 3/2$) three-quantum coherence. Coherence counting experiments demonstrate that four- and two-quantum coherences evolve during t_1. The heteronuclear spinning-sideband patterns observed for the three-spin H–Na–H system associated with the Na(2) site are analyzed. For an IS_2 system, simulated spectra show that, considering the free parameters, the spinning-sideband patterns are particularly sensitive to only, first, the angle between the two IS internuclear vectors and, second, the two heteronuclear dipolar couplings. It is demonstrated that the proton localization around the Na(2) site according to the literature crystal structure of Na_2HPO_4 is erroneous. Instead, the experimental data is consistent with two alternative different structural arrangements, whereby either there is a deviation of 10° from linearity for the case of two identical Na–H distances, or there is a linear arrangement, but the two Na–H distances are different. Furthermore, the question of the origin of spinning-sidebands in the (homonuclear) MQ MAS experiment is revisited. It is shown that the asymmetric experimental MQ sideband pattern observed for the low-C_Q Na(2) site in Na_2HPO_4 can only be explained by considering the ^{23}Na chemical shift anisotropy. © 2002 Elsevier Science

Key Words: **MQ MAS; REDOR recoupling; rotor-encoded spinning-sideband patterns; half-integer quadrupolar nuclei; heteronuclear correlation.**

INTRODUCTION

In solid-state NMR, anisotropic interactions, e.g., the chemical shift anisotropy (CSA) and the dipolar and quadrupolar couplings, lead to a broadening of the resonances, which, on the one hand, has the disadvantage of hindering the resolution of distinct sites, but, on the other hand, contains valuable structural and dynamic information (*1–3*). The challenge facing the solid-state NMR spectroscopist is then how can experiments be designed which combine high resolution with the preservation of the valuable information inherent to the anisotropic interactions.

In recent years, much progress has been made with regards to achieving high resolution in both half-integer quadrupolar nuclei and ^1H solid-state NMR. For half-integer quadrupolar nuclei, a residual second-order quadrupolar broadening of the central transition which cannot be fully removed by magic-angle spinning (MAS) alone often prevents the resolution of resonances due to chemically or crystallographically distinct sites (*4*). In 1995, Frydman and Harwood presented a two-dimensional multiple-quantum (MQ) MAS experiment, which, by means of the formation of an echo corresponding to the refocusing of the residual (fourth-rank) second-order quadrupolar broadening, yields two-dimensional spectra in which anisotropically broadened ridges are resolved on the basis of their different isotropic chemical and second-order quadrupolar shifts (*5*). In this way, the experiment satisfies the criterion introduced above of achieving high resolution while allowing the extraction of the parameters describing the anisotropic broadening. It is to be noted that the experiment is only applicable for odd MQ orders (e.g., 3Q or 5Q), for which there is no first-order quadrupolar broadening. This method has the big advantage of requiring only conventional MAS hardware. In the past five years, much attention has been devoted to the optimization of the technique, with respect to, e.g., obtaining pure absorption-mode lineshapes, improving

[1] This work was presented at the 42nd Experimental NMR Conference, Orlando, Florida, March 11–16, 2001.

[2] Present address: Technical University, Physics Department, R-3400 Cluj, Romania.

[3] Present address: Laboratoire de Stéréochimie et des Interactions Moléculaires, UMR-5532 CNRS/ENS, Ecole Normale Supérieure de Lyon, 69364 Lyon, France.

[4] To whom correspondence should be addressed.

1090-7807/02 $35.00

the sensitivity, and extending the applicability to nuclei with ever greater quadrupolar couplings; various groups have carried out studies to compare the different variants which have been proposed (*6–8*). The development has been so rapid that MQ MAS NMR of nuclei such as ^{23}Na (spin $I = 3/2$), ^{27}Al (spin $I = 5/2$), and ^{17}O (spin $I = 5/2$) can now be considered to be routine, with many applications having been presented, which encompass, e.g., glasses, minerals, and microporous materials (*9–14*).

^{1}H NMR of rigid solids is complicated by the homonuclear proton–proton dipolar interaction; this leads to a substantial homogeneous broadening, which is only partially narrowed by MAS, with the degree of line narrowing increasing upon increasing the MAS frequency, ν_R. Until recently, the maximum typically achievable ν_R was $\sim$15 kHz; at such a ν_R, the resolution in a ^{1}H MAS NMR spectrum of a rigid solid is inadequate. The past three years have, however, seen the introduction of MAS probes, which, by reducing the rotor diameter, allow the routine realization of a ν_R in excess of 25 kHz. At these very fast ν_R, a number of examples have shown that the line narrowing is sufficient to permit ^{1}H resonances due to particular chemically distinct protons to be distinguished (*15–21*). The combination of MAS with two-dimensional MQ spectroscopy has also been shown to be of great value in ^{1}H solid-state NMR, with double-quantum (DQ) MAS NMR (*22*) allowing the structural and dynamic information inherent to proton–proton dipolar couplings to be probed (*15–19*).

Solid-state NMR is, of course, not restricted to homonuclear experiments, with heteronuclear experiments which involve coherence transfer between different types of nuclei providing much important insight. For spin $I = 1/2$ nuclei, heteronuclear ^{1}H–^{13}C correlation experiments allow the better resolution and assignment of the ^{1}H resonances, by taking advantage of, first, the much greater resolution in the ^{13}C dimension on account of the larger chemical shift range and inherently narrower linewidths, and, second, the comparative insensitivity of ^{13}C chemical shifts to through-space influences. Recently, three different methods for recording high-resolution ^{1}H–^{13}C correlation spectra have been proposed (*23–29*). While two of the methods (*23–26*) use a homonuclear dipolar decoupling scheme, namely frequency-switched Lee-Goldburg (FSLG) (*30*), at a moderate ν_R, to achieve narrow ^{1}H linewidths, the method due to Saalwächter *et al.* (*27–29*) simply makes use of brute-force very fast MAS. In addition, the methods differ in the means by which coherence transfer is achieved. The first (*23*) and last (*27–29*) approaches both make use of the heteronuclear dipolar couplings. The transfer mechanism is different in the two cases; polarization transfer under rotational-echo double-resonance (REDOR) recoupling (*31*) in the latter case allows largely selective, i.e., one-bond, transfer with a high sensitivity. This is not the case with the simple cross-polarisation (CP) step employed by Van Rossum *et al.* (*23*), although it is to be noted that the selectivity can be much improved using CP at the LG condition (*32*). By comparison, the method developed by Emsley and co-workers (*24–26*) utilizes the isotropic through-bond J coupling.

Since the dipolar coupling has an inverse cubed dependence on the internuclear separation, solid-state NMR experiments which allow the quantitative determination of particular dipolar couplings provide much structural insight. For spin $I = 1/2$ nuclei, the REDOR technique (*31*) is well established as a method for determining heteronuclear dipolar couplings, and hence distances, between pairs of specifically labeled nuclei (often ^{13}C and ^{15}N). Recently, renewed attention has focused on the development of methods suitable for the measurements of heteronuclear dipolar couplings between protons and other spin $I = 1/2$ nuclei (i.e., ^{13}C–^{1}H and ^{15}N–^{1}H) (*32–36*). The advantage of inverse detection in ^{15}N–^{1}H experiments has been demonstrated (*20, 37*).

The qualitative and quantitative probing of proximities between half-integer quadrupolar and spin $I = 1/2$ nuclei is also of much interest. Indeed, the ability of the MQ MAS method to achieve high resolution for half-integer quadrupolar nuclei has stimulated the development of experiments which provide access to the structural information inherent to the heteronuclear dipolar couplings between half-integer quadrupolar and spin $I = 1/2$ nuclei. For example, the introduction of a CP step from ^{1}H or ^{19}F to a half-integer quadrupolar nucleus, e.g., ^{23}Na, ^{27}Al, ^{17}O, or ^{45}Sc, achieves a spectral editing, whereby signal is only observed for those quadrupolar nuclei having a close proximity to the spin $I = 1/2$ nucleus. In the first examples of this approach, CP to ^{27}Al single-quantum (SQ) coherence was followed by a selective 90° pulse which created a population difference across the $m = \pm 1/2$ central transition, from which MQ coherence was excited as in a usual MQ MAS experiment (*38, 39*). Subsequently, it has been shown that CP direct to the MQ coherences of a half-integer quadrupolar nucleus is possible (*40–46*). Wang *et al.* have also presented a ^{23}Na–^{31}P heteronuclear experiment, where an isotropic ^{23}Na dimension is correlated with a SQ ^{31}P dimension via a CP step (*47*).

Recently, Fernandez *et al.* (*48*) and Pruski *et al.* (*49*) demonstrated how the combination of the MQ MAS and REDOR methods allows the quantitative determination of ^{19}F–^{27}Al dipolar coupling constants, and hence ^{19}F–^{27}Al distances, for each of the three distinct Al sites in a fluorinated aluminophosphate. The experiments described in the two papers differ with regard to the ^{27}Al coherence order whose evolution is subjected to the REDOR pulses: the authors use the terminology 3Q-t_1-REDOR and 3Q-t_2-REDOR to distinguish between dephasing of ^{27}Al 3Q and SQ coherences, respectively. The former approach has the advantage that the dephasing of 3Q coherence is three times more sensitive to the heteronuclear dipolar coupling constant. This advantage comes, however, at the cost of sensitivity losses associated with the required inversion of the half-integer quadrupolar nucleus MQ coherence.

In this paper, we present a new experimental method whereby a half-integer quadrupolar 3Q and spin $I = 1/2$ SQ heteronuclear coherence is allowed to evolve during t_1: in analogy to the methods developed by Saalwächter *et al.* for dipolar-coupled pairs of spin $I = 1/2$ nuclei (*27–29*), this heteronuclear

coherence is generated by the application of a spin $I = 1/2$ 90° pulse to the mixed state produced by the REDOR-recoupled evolution of half-integer quadrupolar 3Q coherence under the heteronuclear dipolar coupling. The approach is related to the 3Q-t_1-REDOR experiment due to Pruski *et al.* (*49*) with the important distinction that, since a heteronuclear coherence containing spin $I = 1/2$ SQ coherence is actually created, a second REDOR-recoupling period must be applied after t_1 to recreate homonuclear 3Q coherence. As a motivation for this work, we further acknowledge the 6Q experiment presented by Duer and Painter, in which dipolar-coupled pairs of ^{23}Na nuclei are observed (*50*).

The t_1 evolution of the heteronuclear MQ coherence is correlated with, in t_2, the evolution of half-integer quadrupolar SQ coherence, such that anisotropically broadened ridges are resolved on the basis of their different isotropic chemical and second-order quadrupolar shifts as in the usual MQ MAS experiment. In this way, the ability of the homonuclear MQ MAS experiment to achieve high resolution is combined with a spectral editing based on the proximity of the particular half-integer quadrupolar nucleus to a spin $I = 1/2$ nucleus. As compared to the CP methods described above, this approach has the advantage that, first, the required recycle delay is that of the quadrupolar rather than the spin $I = 1/2$ nucleus, and, second, the coherence transfer occurs in a more controlled fashion.

Provided that the t_1 increment is not rotor-synchronized, a heteronuclear MQ MAS spinning-sideband pattern is observed in F_1. For MQ MAS spectroscopy of dipolar-coupled pairs of spin $I = 1/2$ nuclei, it is well established that the appearance of a MQ MAS spinning-sideband pattern is determined predominantly by the rotor encoding of the dipolar interaction (*51–53*). For example, it has been shown that the ability to quantitatively extract the dipolar coupling by means of an analysis of MQ MAS spinning-sideband patterns enables the order parameters for different discotic liquid-crystalline phases to be determined, with the method having been demonstrated for both homonuclear (^{1}H–^{1}H) (*16*) and heteronuclear (^{1}H–^{13}C) (*33*) dipolar-coupled nuclei. In addition, an analysis of ^{1}H–^{1}H double-quantum (DQ) MAS spinning-sideband patterns has been shown to allow the quantitative determination of proton–proton distances within the complex hydrogen-bonded arrangement in the biologically important molecule, bilirubin (*19*). Moreover, Gregory *et al.* have demonstrated that the rotor encoding of the CSA in ^{13}C–^{13}C DQ MAS spinning-sideband patterns permits the elucidation of the mutual orientation of CSA tensors (*54*).

We show, here, that the sideband patterns obtained for the heteronuclear MQ MAS experiment are sensitive not only to the dipolar coupling constant, but also to the quadrupolar coupling as well as, for an isolated spin pair, the orientation of the quadrupolar principal axes system (PAS) with respect to the internuclear vector, which defines the dipolar PAS. Since the quadrupolar coupling can be determined in a conventional MQ MAS experiment, an analysis of the heteronuclear MQ MAS spinning-sideband patterns provides access to the dipolar coupling as well as the relative orientation of the quadrupolar PAS. For an IS_2 spin system, it is shown that, considering the free parameters, the spinning-sideband patterns are particularly sensitive to only, first, the angle between the two IS internuclear vectors and, second, the two heteronuclear dipolar couplings.

1. THE QUADRUPOLAR AND DIPOLAR HAMILTONIANS

To begin with, we introduce the analytical framework with which the presented experiments will be described. For nuclei for which the MQ MAS experiment is of relevance, the quadrupolar Hamiltonian, H_Q, can be treated as a weak perturbation of the Zeeman interaction. As described in Refs. (*55, 56*) H_Q can then be determined using average Hamiltonian theory (*57*). Without any loss of generality, the simplifying assumption that the asymmetry parameter, η, equals 0 can be made. Under MAS,

$$H_Q(t) = H_Q^{(1)}(t) + H_Q^{(2)}(t), \qquad [1]$$

where

$$H_Q^{(1)}(t) = \omega_Q^{PAS} \sum_{-2}^{2} D_{0m}^2(\alpha, \beta, \gamma) \times D_{m0}^2(\omega_R t, \theta_M, 0)\left\{I_Z^2 - I(I+1)/3\right\} \qquad [2]$$

and

$$H_Q^{(2)}(t) = \frac{2\left(\omega_Q^{PAS}\right)^2}{9\omega_0}\{L + M + N\}, \qquad [3]$$

with

$$L = \frac{3}{5} I_Z \left\{3I_Z^2 - I(I+1)\right\} \qquad [4]$$

$$M = \frac{3}{14} \sum_{-2}^{2} D_{0m}^2(\alpha, \beta, \gamma) D_{m0}^2(\omega_R t, \theta_M, 0) \times I_Z\left\{12I_Z^2 - 8I(I+1) + 3\right\} \qquad [5]$$

$$N = \frac{9}{70} \sum_{-4}^{4} D_{0m}^4(\alpha, \beta, \gamma) D_{m0}^4(\omega_R t, \theta_M, 0) \times I_Z\left\{-34I_Z^2 + 18I(I+1) - 5\right\}. \qquad [6]$$

Here, ω_R and θ_M denote the MAS frequency (in angular units) and the magic angle (equal to $\arctan(\sqrt{2}) = 54.7°$), respectively, while the Euler angles (α, β, γ) relate the principal axes system of the quadrupolar tensor to the rotor frame. The $D_{mn}^l(\alpha, \beta, \gamma)$

terms are Wigner matrix elements (*58*). The quadrupolar frequency, ω_Q^{PAS}, is given by

$$\omega_Q^{PAS} = \frac{3e^2qQ}{4I(2I-1)\hbar} = \frac{3\pi C_Q}{2I(2I-1)}, \quad [7]$$

where C_Q is the quadrupolar coupling constant (in units of Hz). For the second-order term, a useful approximation which will be employed here is to consider the average over an integral number of rotor periods. For periods of free evolution, this corresponds to a rotor-synchronized experiment, in which all spinning sidebands can be considered to fold onto the centerband position. In this case, the average of the $D^l_{m0}(\omega_R t, \theta_M, 0)$ term is only nonzero if $m = 0$, and Eq. [3] simplifies to

$$H_Q^{(2)} = \frac{2\left(\omega_Q^{PAS}\right)^2}{9\omega_0}\{L + N'\}, \quad [8]$$

where

$$N' = \frac{9}{70} d^4_{00}(\beta)\, d^4_{00}(\theta_M) I_Z \left\{-34I_Z^2 + 18I(I+1) - 5\right\}. \quad [9]$$

Equation [8] is a good approximation also for evolution periods of arbitrary length, provided that the second order quadrupolar interaction is significantly smaller than the MAS frequency.

For an isolated pair of nuclei, the heteronuclear dipolar Hamiltonian is given as

$$H_D(t) = 2\omega_D(t) I_Z S_Z, \quad [10]$$

where

$$\omega_D(t) = -D_{IS} \sum_{-2}^{2} D^2_{0m}(\psi, \theta, \varphi) D^2_{m0}(\omega_R t, \theta_M, 0), \quad [11]$$

with the dipolar coupling constant (in angular frequency units) being defined as

$$D_{IS} = \frac{\mu_0}{4\pi} \frac{\gamma_I \gamma_S}{r_{IS}^3} \hbar. \quad [12]$$

The Euler angles (ψ, θ, φ) relate the principal axes system of the dipolar coupling tensor to the rotor frame, and r_{IS} represents the internuclear distance between the I and S nuclei, with γ denoting the magnetogyric ratio of the nucleus.

According to the Liouville–von Neumann equation, the evolution of the density operator, $\rho(t)$, is described by

$$\rho(t_b) = U(t_b, t_a)\rho(t_a)U^+(t_b, t_a), \quad [13]$$

where

$$U(t_b, t_a) = T \exp\left\{-i \int_{t_a}^{t_b} H(t)\, dt\right\}, \quad [14]$$

with T being the Dyson time-ordering operator. The superoperator notation

$$\hat{U}\rho \equiv U\rho U^+ \quad [15]$$

will be used in all subsequent calculations of the spin system evolution. In the following, the eigenstates $|m_I\rangle$ of the I-spin Zeeman Hamiltonian are chosen as basis functions for the density operator.

In the following, we make the assumption that the quadrupolar and dipolar Hamiltonians commute such that the total propagator can be factorized into separate quadrupolar and dipolar terms. In this context, it is to be noted that Wu and Wasylishen have shown, for the case of a spin $I = 3/2$ nucleus dipolar coupled to a spin $I = 1/2$ nucleus, that there is no residual broadening due to second-order quadrupolar–dipolar effects in MQ MAS NMR spectra where only symmetric transitions (i.e., the central transition SQ and 3Q coherences) are involved (*59*). This is to be contrasted with the case where two quadrupolar nuclei are dipolar coupled together (*60–62*).

Considering first the quadrupolar interaction, it can be shown (see Appendix) that the propagator is given by

$$U_Q(t_b, t_a) = \sum |m_I\rangle\langle m_I| \exp\left\{-i \int_{t_a}^{t_b} \langle m_I|H_Q(t)|m_I\rangle\, dt\right\}. \quad [16]$$

Note that the terms $\langle m_I|H_Q(t)|m_I\rangle$ correspond to the diagonal elements of the matrix representation of the quadrupolar Hamiltonian.

The propagator for the dipolar interaction for an IS spin pair is similarly given as

$$U_D(t_b, t_a) = \sum |m_I\rangle\langle m_I| \exp\{-i2\langle m_I|I_Z S_Z|m_I\rangle \Omega_D(t_b, t_a)\} = \sum |m_I\rangle\langle m_I| \exp\{-i2m_I S_Z \Omega_D(t_b, t_a)\}, \quad [17]$$

where

$$\Omega_D(t_b, t_a) = \int_{t_a}^{t_b} \omega_D(t)\, dt. \quad [18]$$

By performing an integration for the summation of terms given in Eq. [11], using the explicit expressions for the Wigner matrix

elements (*58*), it can be shown that the dipolar phase is given by:

$$\Omega_D(t_b, t_a) = \frac{D_{IS}}{\omega_R}\left\{\frac{1}{\sqrt{2}}\sin(2\theta)[\sin(\omega_R t_b+\varphi)-\sin(\omega_R t_a+\varphi)] - \frac{1}{4}\sin^2(\theta)[\sin(2\omega_R t_b+2\varphi)-\sin(2\omega_R t_a+2\varphi)]\right\}. \quad [19]$$

2. EXPERIMENTAL AND SIMULATION DETAILS

Experimental results were obtained for a sample of dibasic sodium phosphate (Riedel–de Haën AG, 99% purity), Na_2HPO_4. In Ref. (*63*) the characterisation of Na_2HPO_4 by solid-state ^{23}Na MAS NMR and powder X-ray diffraction is described. The so-determined ^{23}Na (spin $I = 3/2$) quadrupolar coupling constants and asymmetry parameters for the three crystallographically distinct sodium sites are listed in Table 1. A fit of the anisotropic lineshapes obtained in a later MQ MAS investigation yielded, within the experimental error, the same quadrupolar parameters (*64*). From the refined crystal structure presented in Ref. (*63*), each sodium nucleus is found to have two nearby protons; Table 2 lists the Na–H distances and H–Na–H angles (the next nearest protons are over 0.4 nm away). It is to be noted, though, that the proton positions in the structure were determined by merely chemical arguments, since "attempts to locate the proton by calculation of the residual electron density failed." This is a common problem of X-ray diffraction; since X-rays are scattered by electrons, the localization of hydrogen atoms, which have the lowest electron density of all elements, is very difficult.

NMR experiments were performed on a Bruker ASX 500 wide-bore spectrometer, operating at ^1H and ^{23}Na Larmor frequencies of 500.1 and 132.3 MHz, respectively, using a double-resonance MAS probe supporting a rotor of outer diameter 2.5 mm. For ^1H, the 90° pulse length was set equal to either 2.0 or 2.2 μs. For ^{23}Na, a power level was chosen which gave an optimized 3Q excitation pulse of 3.5 μs and a 3Q inversion pulse of 3.0 μs. At this power level, setting the 3Q to 1Q conversion pulse to 1.75 μs led to the signals originating from the $p = +3$ to $p = -1$ and $p = -3$ to $p = -1$ pathways (where p is the coherence order) having equal amplitudes (as demonstrated by a coherence counting experiment in Section 5). As discussed in Refs. (*6, 65*). this pulse length of 1.75 μs corresponds to the ^{23}Na 90° flip angle.

TABLE 1
^{23}Na Quadrupolar Parameters for Na_2HPO_4 (*63*)

Sodium Site	C_Q/MHz	η
1	2.1	0.7
2	1.4	0.2
3	3.7	0.3

TABLE 2
Na–H Distances and H–Na–H Angles in Na_2HPO_4 (*63*)

Sodium Site	Na–H distance/nm	Na–H (D/2π)/kHz	H–Na–H angle/°
1	0.279	1.46	180
	0.279	1.46	
2	0.270	1.62	180
	0.270	1.62	
3	0.260	1.83	81
	0.269	1.63	

The ^1H MAS ($\nu_R = 30$ kHz) spectrum (not shown) is dominated by a relatively sharp (full width at half-maximum height of 250 Hz) peak at 12.7 ppm. Other spectral features, principally a broad hump of weak intensity centered at about 7 ppm, were not observed in a 1D DQ filtered spectrum, obtained using a compensated BABA recoupling pulse sequence (*66*) of duration 2 τ_R (where τ_R denotes a rotor period) at $\nu_R = 30$ kHz. The ^1H rf transmitter frequency was set to be on resonance with the peak at 12.7 ppm for all experiments.

Time-domain density matrix simulations were performed using the SIMPSON NMR simulation program (*67*). Representative input files are given in the Appendix.

3. AN ANALYTICAL DESCRIPTION OF THE 3Q MAS EXPERIMENT

An important feature of the heteronuclear MQ MAS experiment is that the ability of the homonuclear MQ MAS experiment to achieve high resolution is retained. In order to illustrate this, in this section, we, first, briefly review the homonuclear MQ MAS technique, and show mathematically how the residual second-order quadrupolar broadening is refocused.

The pulse sequence and coherence transfer pathway diagram (*68, 69*) for the simplest amplitude-modulated 3Q MAS experiment (*64, 70–72*) is shown in Fig. 1a. As discussed in Refs. (*6, 65*), pure absorption-mode 2D lineshapes are obtained using this experiment, for the case of a spin $I = 3/2$ nucleus, if the 3Q to 1Q conversion pulse is set equal to 90°. It is to be noted that other approaches for obtaining pure absorption-mode 2D lineshapes have been proposed, such as the incorporation of a z filter (*73, 74*) or the acquisition of a whole echo (*72, 75*); a comparison of these different approaches is presented in Ref. (*6*). In addition, much attention has been focused on optimizing the sensitivity of the coherence transfer processes, for example, the use of a double frequency sweep (DFS) (*76*) or a fast amplitude-modulated (FAM) pulse (*77*) has recently been shown to significantly improve the sensitivity of the 3Q to 1Q step. In this paper, in order to demonstrate the feasibility of the REDOR-recoupled heteronuclear MQ MAS experiment, we have chosen to adapt the simple amplitude-modulated 3Q MAS experiment in Fig. 1a. The possibility of improving the experimental sensitivity by

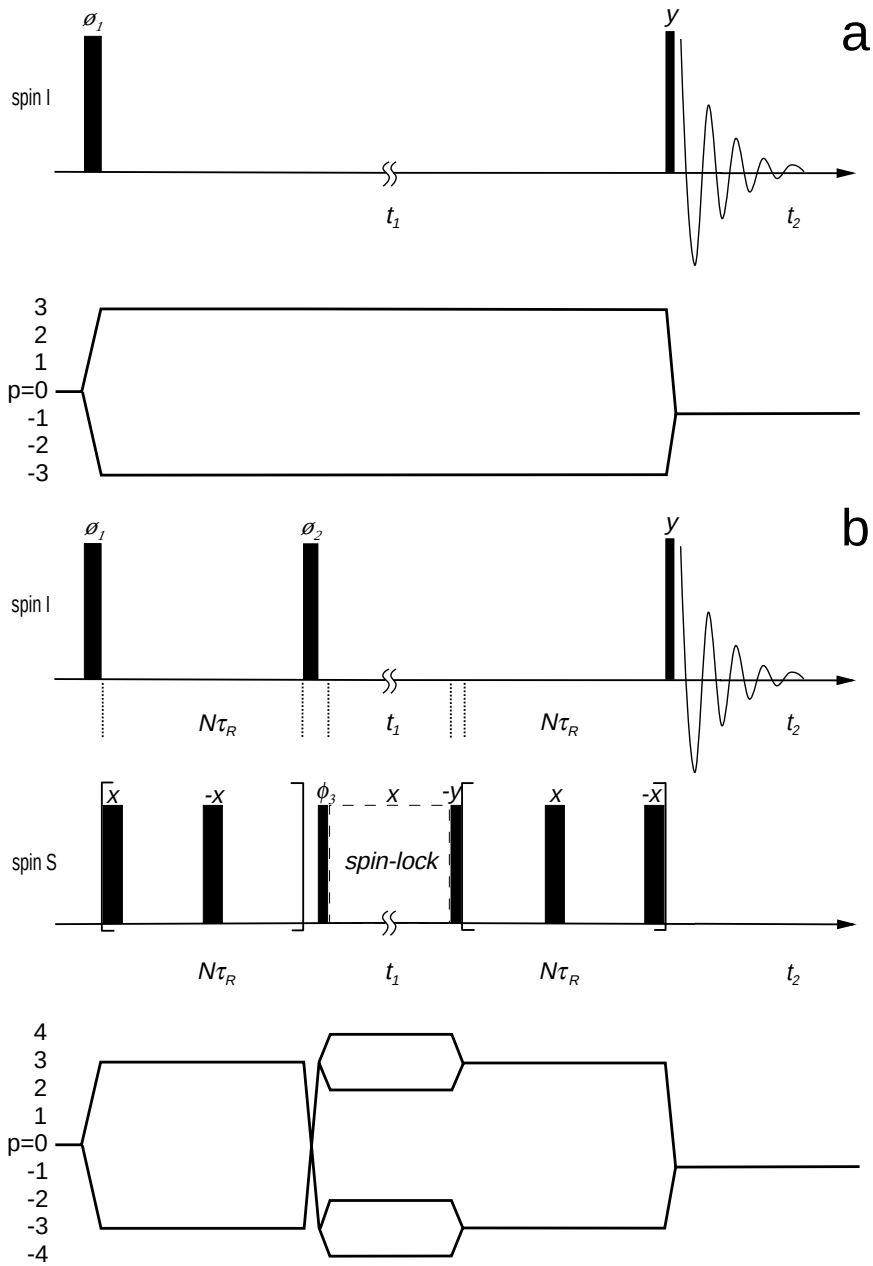

FIG. 1. Pulse sequences and coherence-transfer pathway diagrams for (a) the simple (two-pulse) amplitude-modulated MQ MAS experiment and (b) an amplitude-modulated heteronuclear MQ MAS experiment. The widths of the rectangular blocks denoting radiofrequency pulses are proportional (for the separate I and S channels) to the pulse flip angles. In both cases, spin I (^{23}Na) 3QC is initially created by a single pulse of flip angle $\sim$240°, and finally converted into spin I (^{23}Na) SQC by a single pulse of flip angle 90°. In (b), heteronuclear MQC (both ±2 and ±4) is created by the application of a spin S (^{1}H) 90° pulse to a state created by evolution under the IS dipolar coupling, using REDOR recoupling (spin S (^{1}H) 180° pulses applied at $\tau_R/2$ intervals); the application of the same sequence of pulses and delays in reverse recreates homonuclear spin I (^{23}Na) 3QC. Evolution of spin I coherence under chemical and quadrupolar shifts during the two REDOR recoupling periods is refocused by a 180° pulse applied before the start of t_1. The spin S (^{1}H) 180° pulses at the start of the period before t_1 and at the end of the period after t_1 may be omitted for the first and last rotor period of recoupling, respectively. A ^{1}H spin lock may be applied during t_1. A phase cycling scheme for the phases ϕ_1, ϕ_2, ϕ_3 and that of the receiver, R_x, in (b) is given in Table 3 (see Section 5).

incorporating, e.g., DFS or FAM pulses and whole-echo acquisition is discussed in the concluding section.

Here, we consider the 3Q MAS experiment for a spin $I = 3/2$ nucleus using the analytical framework introduced above. First, it is necessary to calculate the evolution of central-transition SQ coherence (SQC), $|\pm1/2\rangle\langle\mp1/2|$, and 3Q coherence (3QC), $|\pm3/2\rangle\langle\mp3/2|$, under the quadrupolar Hamiltonian. (Note that the satellite SQCs are neglected, since they, unlike the

central-transition SQC, are broadened to first-order by the quadrupolar coupling. The corresponding signals in a powder frequency-domain spectrum are spread over a frequency range on the order of a MHz, and can hence be assumed to be lost in the spectral baseline.) Using Eqs. [15] and [16] and remembering the orthonormality of the eigenstates $|m_I\rangle$,

$$\begin{aligned}\hat{U}_Q(t_b, t_a)\ &|\pm m_I\rangle\langle\mp m_I| \\ &= \exp\left\{ i \int_{t_a}^{t_b} \langle\mp m_I|H_Q(t)|\mp m_I\rangle\, dt \right. \\ &\quad \left. -i \int_{t_a}^{t_b} \langle\pm m_I|H_Q(t)|\pm m_I\rangle\, dt \right\} |\pm m_I\rangle\langle\mp m_I|. \quad [20]\end{aligned}$$

Equations [1]–[9] express the quadrupolar Hamiltonian, H_Q, using average Hamiltonian theory. It can then be shown that the first-order terms in Eq. [20] vanish, leaving only second-order terms. Considering the approximation corresponding to taking an average over an integral number of rotor periods (Eqs. [8] and [9]),

$$\begin{aligned}\hat{U}_Q(t_b, t_a)&|\pm 1/2\rangle\langle\mp 1/2| \\ &= \exp\{\mp i\, A(-7 + 27B)(t_b - t_a)\}|\pm 1/2\rangle\langle\mp 1/2| \quad [21]\end{aligned}$$

$$\begin{aligned}\hat{U}_Q(t_b, t_a)&|\pm 3/2\rangle\langle\mp 3/2| \\ &= \exp\{\mp i\, A(21 - 21B)(t_b - t_a)\}|\pm 3/2\rangle\langle\mp 3/2|, \quad [22]\end{aligned}$$

where

$$A = \frac{2\left(\omega_Q^{PAS}\right)^2}{35\omega_0} \quad [23]$$

$$B = d_{00}^4(\beta) d_{00}^4(\theta_M). \quad [24]$$

In the 3Q MAS experiment in Fig. 1a, a single pulse (*64, 70–73, 78–80*) is used to convert I_Z equilibrium magnetization into 3QC, which is selected by a suitable phase cycle. This 3QC evolves during t_1 and is subsequently converted by a 90° pulse into central transition SQC (by convention, the use of quadrature detection corresponds to the selection of $p = -1$ coherence), which is detected in the second evolution period t_2. The time-domain signal, $S(t_1, t_2)$, is thus described as

$$S(t_1, t_2) = S_{-3}(t_1, t_2) + S_3(t_1, t_2), \quad [25]$$

where

$$\begin{aligned}S_{-3}(t_1, t_2) &= \Lambda_0^{-3} \exp\{+i\, A(21 - 21B)t_1\} \\ &\quad \times \Lambda_{-3}^{-1} \exp\{+i\, A(-7 + 27B)t_2\} \quad [26]\end{aligned}$$

$$\begin{aligned}S_{+3}(t_1, t_2) &= \Lambda_0^{+3} \exp\{-i\, A(21 - 21B)t_1\} \\ &\quad \times \Lambda_{+3}^{-1} \exp\{+i\, A(-7 + 27B)t_2\}. \quad [27]\end{aligned}$$

It is to be noted that the isotropic chemical shift is not taken into account in the above equations. In addition, the pulses are considered to have negligible duration (the validity of this approximation is considered in Section 8); the coherence transfer amplitude for a given pulse is labeled by Λ_m^n, where m and n are the initial and final coherence orders, respectively. For a 90° pulse, $\Lambda_{-3}^{-1} = \Lambda_{+3}^{-1}$ for all crystallite orientations, and the signal is amplitude-modulated with respect to t_1

$$\begin{aligned}S(t_1, t_2) &= 2\Lambda_{exc}\Lambda_{conv} \cos\{A(21 - 21B)t_1\} \\ &\quad \times \exp\{+i\, A(-7 + 27B)t_2\}, \quad [28]\end{aligned}$$

where Λ_{exc} and Λ_{conv} denote the coherence transfer amplitudes for the excitation and conversion pulses, respectively.

The beauty of the MQ MAS experiment is illustrated by Eq. [26], which corresponds to the time-domain signal for the so-called echo pathway (for a discussion of echo and antiecho pathways in the MQ MAS experiment, the reader is referred to Ref. (*6*)); at times $t_2 = 7t_1/9$, the fourth-rank anisotropic broadening, denoted by B, is refocused, while, importantly, the isotropic second-order quadrupolar shift, denoted by A, and the isotropic chemical shift are not refocused. (As described in, e.g., Ref. (*6*), the same applies for the case of a nonzero asymmetry parameter.) A 2D frequency-domain spectrum obtained using the amplitude-modulated experiment in Fig. 1a (the time-domain signal for a single nuclear site being described by Eq. [28]) consists of pure absorption-mode anisotropically broadened ridges, each with a slope of $-7/9$ with respect to the ω_2 axis, which are resolved according to their different isotropic (both chemical and second-order quadrupolar) shifts.

4. AN ANALYTICAL DESCRIPTION OF THE HETERONUCLEAR MQ MAS EXPERIMENT

The pulse sequence and coherence transfer pathway diagram (the total combined coherence order is represented) for a heteronuclear amplitude-modulated 3Q MAS experiment is shown in Fig. 1b, with spins I and S referring to the spin $I = 3/2$ and the $I = 1/2$ nucleus, respectively. As in the 3Q MAS experiment in Fig. 1a, a single pulse initially creates spin I 3QC, while a final spin I 90° pulse converts spin I 3QC into detectable spin I central transition SQC, with equal amplitude for the two pathways. Immediately following the 3Q excitation pulse and immediately preceding the 3Q to SQ conversion pulse, there are two periods of REDOR (*31*) recoupling—180° pulses applied on the spin S channel every $\tau_R/2$—which counteract the averaging of the heteronuclear IS dipolar coupling by MAS. In addition, the insertion of a 3Q inversion pulse at the end of the first REDOR recoupling period ensures that the evolution of the spin I 3QC

under all spin I shifts (i.e., both the isotropic and anisotropic quadrupolar and the isotropic chemical shifts) is refocused at the end of the second REDOR recoupling period. Thus, only evolution under the heteronuclear IS dipolar coupling needs to be considered during the two recoupling periods.

Recently, Saalwächter *et al.* have presented a related series of heteronuclear MQ MAS experiments which are applicable to dipolar-coupled spin $I = 1/2$ nuclei (*27–29*). In particular, a distinction was made with respect to whether the initial (after any preparation, i.e., CP, step) and the finally detected magnetization states were of the same nuclear species or not, with asymmetric and symmetric sequences being termed recoupled polarization transfer (REPT) (*27, 28*) and dipolar heteronuclear multiple-spin correlation (DIP-HMSC) (*29*), respectively. By this classification system, the pulse sequence presented here is of the latter symmetric type.

To analytically describe this experiment, it is first necessary to calculate the evolution of spin I 3QC under the heteronuclear dipolar Hamiltonian (as stated above, it is assumed that the dipolar and quadrupolar Hamiltonians commute, such that the evolution under the two interactions can be considered separately). In the following, an isolated IS spin pair is considered. Using Eqs. [15] and [17] and remembering the orthonormality of the eigenstates $|m_I\rangle$,

$$\begin{aligned}\hat{U}_D(t_b, t_a)&|\pm 3/2\rangle\langle\mp 3/2| \\ &= \exp\{\mp 6i S_Z \Omega_D(t_b, t_a)\}|\pm 3/2\rangle\langle\mp 3/2| \\ &= \{\cos(3\Omega_D(t_b, t_a)) \mp 2i \sin(3\Omega_D(t_b, t_a))S_Z\}|\pm 3/2\rangle\langle\mp 3/2|.\end{aligned} \quad [29]$$

Eq. [29] is derived by, first, expanding the exponential term as a power series. After using the identity ${S_z}^2 = \mathbf{I}/4$ (where $\mathbf{I}$ is the identity matrix), the resulting expression can be identified to consist of two power series corresponding to the trigonometric terms in Eq. [29]. For a recoupling time, τ_{rcpl}, equal to $N\tau_{\mathrm{R}}$ of REDOR recoupling, Eq. [29] can be reexpressed (assuming that the spin *S* pulses are infinitely hard, i.e., of zero duration) as

$$\begin{aligned}\hat{U}_D(N\tau_R, 0)&|\pm 3/2\rangle\langle\mp 3/2| \\ &= \{\cos(6N\Omega_D(\tau_R/2, 0)) \mp 2i \sin(6N\Omega_D(\tau_R/2, 0))S_Z\} \\ &\quad \times |\pm 3/2\rangle\langle\mp 3/2|.\end{aligned} \quad [30]$$

A spin S 90° pulse converts the $|\pm 3/2\rangle\langle\mp 3/2|S_z$ state into a mixture of heteronuclear 4Q coherence, $|\pm 3/2\rangle\langle\mp 3/2|S_+$, and 2Q coherence, $|\pm 3/2\rangle\langle\mp 3/2|S_-$. For an isolated IS spin pair, this heteronuclear coherence only evolves under the spin I quadrupolar coupling (and also the spin I and spin S chemical shifts, which are, for simplicity, neglected in this calculation). The spin S 90° pulse which follows t_1 and the second REDOR recoupling period recreate a pure spin I 3QC state. Using Eqs. [21], [22], and [30] and considering the selection of the coherence transfer pathways shown in Fig. 1b, the total time-domain signal (again making the assumption that the spin-I pulses are of negligible duration, with only the coherence transfer amplitudes being considered), thus, takes the form

$$S(t_1, t_2) = S_D(t_1)S_Q(t_1, t_2), \quad [31]$$

where

$$\begin{aligned}S_D(t_1) &= \sin\{6N\Omega_D(\tau_R/2, 0)\}\sin\{6N\Omega_D(\tau_R/2 + t_1, t_1)\} \\ &= \sin\left\{\frac{6\sqrt{2}ND_{IS}}{\omega_R}\sin(2\theta)\sin(\varphi)\right\} \\ &\quad \times \sin\left\{\frac{6\sqrt{2}ND_{IS}}{\omega_R}\sin(2\theta)\sin(\omega_R t_1 + \varphi)\right\}\end{aligned} \quad [32]$$

and

$$\begin{aligned}S_Q(t_1, t_2) &= 2A_{exc}A_{inv}A_{conv}\cos\{A(21 - 21B)t_1\} \\ &\quad \times \exp\{+iA(-7 + 27B)t_2\}.\end{aligned} \quad [33]$$

Eq. [31] demonstrates that the total signal factorises into a quadrupolar and a dipolar contribution. (Such a factorisation is equally achieved for the case of a non-zero asymmetry parameter.) With the addition of the A_{inv} factor, which denotes the coherence transfer amplitude for the 3Q inversion pulse, the quadrupolar contribution mimics the MQ MAS I-spin signal of Eq. [28]. Thus, the virtues of the MQ MAS experiment, namely the refocusing of the residual second-order quadrupolar broadening and, hence, the ability to resolve the anisotropic lineshapes for distinct sites, are preserved. The role of the dipolar term will be explained in the following sections.

5. COHERENCE COUNTING EXPERIMENTS

An investigation of the coherence orders which evolve during the indirect time dimension of a MQ experiment may be carried out by performing a so-called coherence counting experiment (the experiment is usually referred to as a spin-counting experiment due to early applications to the study of dipolar-coupled proton networks (*81*); this terminology is less appropriate here). Using the method presented in Ref. (*82*), this two-dimensional experiment involves recording a series of free-induction decays (FIDs) with $t_1 = 0$, with the phase of all the pulses preceding the t_1 period being successively incremented. It is to be noted that the use of such an approach to observe the build-up of MQ coherence in homonuclear ^{1}H MQ MAS (*83*) and heteronuclear ^{1}H–^{13}C multiple-spin correlation (*29*) experiments has recently been described. To observe a maximum of *n* quantum orders, the phase is varied in $2n$ steps ranging from 0° to 360°. Fourier transformation with respect to the indirect dimension yields a spectrum, where the *n*th line represents the contribution of the *n*th coherence order. Experimentally, it is usual to concatenate

the t_1 "FID" corresponding to phases between 0° to 360°; since there is no relaxation, an artificial linewidth is introduced by applying a weighting function before Fourier transformation. Note that, in order to be able to distinguish between positive and negative coherence orders, it is necessary to use the real and imaginary parts of the t_1 FID. It is to be further noted that the concatenation procedure leads to experimental noise only being observed at positions corresponding to integer coherence orders.

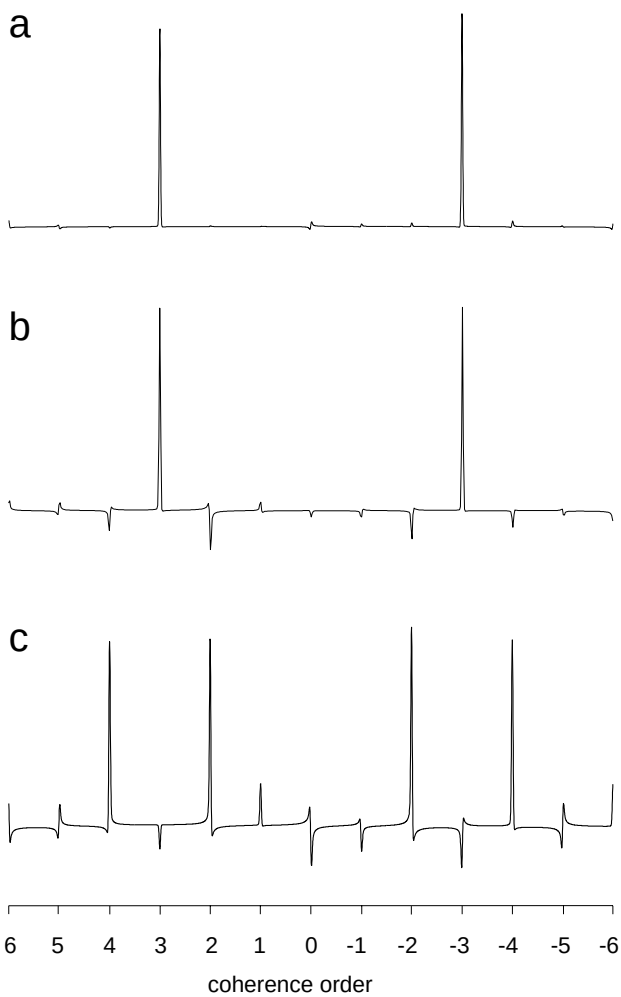

FIG. 2. Spectra obtained from coherence counting experiments performed on Na_2HPO_4 at an MAS frequency of 30 kHz, using (a) the homonuclear (^{23}Na) 3Q MAS and (b) and (c) the heteronuclear (^{23}Na–^{1}H) MQ MAS (with $\tau_{rcpl} = 2\ \tau_R$) pulse sequences in Figs. 1a and 1b, respectively. In all experiments, a six-step phase cycle was applied to select ^{23}Na 3QC. In (b), the ^{23}Na 3Q inversion pulse was additionally phase cycled, while in (c) the full phase cycle given in Table 3 was used. In each case, t_1 was set equal to 2 μs, and a two-dimensional data set (consisting of 12 t_1 points) was recorded by successively incrementing the phases of all pulses before t_1 by 30°. The experimental t_1 "FIDs" where then concatenated 50 times, and a Gaussian weighting function was applied before Fourier transformation; in this way, spectral noise only appears at integral coherence orders. A recycle delay of 2, 2, and 1.5 s was used in (a), (b), and (c), respectively, with 36, 72, and 288 transients being coadded for each phase increment in the respective cases.

TABLE 3
Phase Cycling Scheme for the Heteronuclear MQ MAS Experiment (Fig. 1b)

ϕ_1:	0° 60° 120° 180° 240° 300°
ϕ_2:	12{0°} 12{30°} 12{60°} 12{90°} 12{120°} 12{150°} 12{180°} 12{210°} 12{240°} 12{270°} 12{300°} 12{330°}
ϕ_3:	6{90°} 6{270°}
R_X:	3{0° 180°} 3{180° 0°} 3{180° 0°} 3{0° 180°}

Figure 2 presents the results of coherence counting experiments performed for Na_2HPO_4. In each case, the phase increment was set equal to 30°, such that the maximum observable coherence order, $|p|$, equals 6. The spectrum in Fig. 2a was acquired using the simple amplitude-modulated ^{23}Na MQ MAS experiment (Fig. 1a), while the heteronuclear (^{23}Na-^{1}H) MQ MAS pulse sequence in Fig. 1b was used to record the spectra in Figs. 2b and 2c. The experiments additionally differed with respect to the employed phase cycling scheme (*68, 69*). In all cases, selection of I-spin (^{23}Na) 3QC is achieved by a 6-step phase cycle of the first I-spin pulse. In both heteronuclear MQ MAS experiments (Figs. 2b and 2c), a further 12-step phase cycle of the I-spin (^{23}Na) 3Q inversion pulse selects $\Delta p = \pm 6$. In Fig. 2c only, an additional two step phase cycle of the first S-spin (^{1}H) 90° pulse selects $\Delta p = \pm 1$. The full nested 144-step phase cycle for the heteronuclear MQ MAS experiment in Fig. 1b is given in Table 3.

In Fig. 2a, the spectrum is dominated by the signals at $p = \pm 3$. It was stated above that setting the flip angle of the conversion pulse to 90° leads to an equal contribution of the two pathways, as is required for an amplitude-modulated signal, and hence pure absorption-mode lineshapes. The near equality of the intensities of the $p = +3$ and $p = -3$ signals in Fig. 2a indicates that the experimental pulse length corresponds to (very close to) the desired 90° flip angle. In Fig. 2b, in addition to the strong $p = \pm 3$ signals, weak negative intensity at the $p = \pm 2$ and $p = \pm 4$ positions is observed above the noise level. It is to be noted that the sign of the heteronuclear 2QC and 4QC relative to the homonuclear 3QC depends on the relative phases of the two ^{1}H 90° pulses; when they differ by 180° (as is the case here, see Fig. 1b), the heteronuclear coherences have the opposite sign, while when the phases are the same, the homonuclear and heteronuclear coherences have the same sign. In Fig. 2c, the full 144-step phase cycle blocks pure homonuclear coherence, and only heteronuclear 2QC and 4QC is observed. Although four times as many transients were co-added for the spectrum in Fig. 2c as opposed to that in Fig. 2b, the poorer signal-to-noise (S/N) ratio in Fig. 2c is apparent.

6. THE SENSITIVITY OF THE HETERONUCLEAR MQ MAS EXPERIMENT

Figure 3 compares the ^{23}Na (a) one-pulse spectrum of Na_2HPO_4 with MQ-filtered ($t_1 = 2\mu$s) spectra recorded with

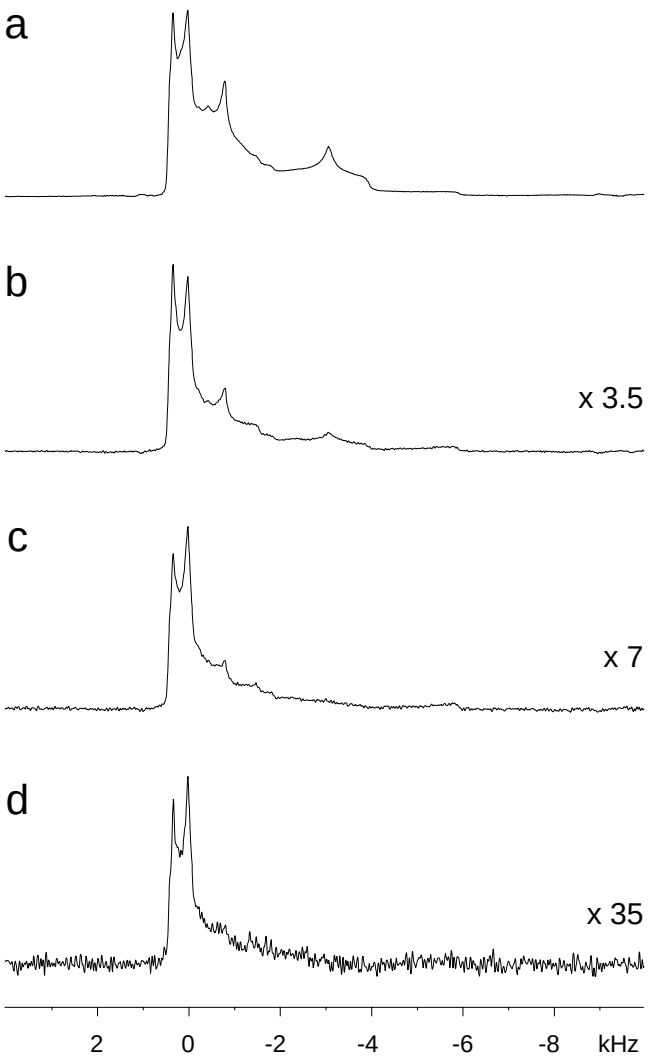

FIG. 3. The ^{23}Na (a) one-pulse spectrum of Na_2HPO_4 is compared with MQ-filtered ($t_1 = 2\ \mu$s) spectra recorded with (b) the homonuclear (^{23}Na) 3Q MAS experiment in Fig. 1a, (c) a homonuclear (^{23}Na) 3Q MAS experiment based on that in Fig. 1a but with a 3Q inversion pulse, and (d) the heteronuclear (^{23}Na–^{1}H) MQ MAS experiment (with $\tau_{rcpl} = 1\ \tau_R$) in Fig. 1b. A MAS spinning frequency of 10 kHz was used. In each case, 1872 transients were coadded and a recycle delay of 4 s was used. The same ^{23}Na pulse durations (see Section 2) were used in all MQ MAS experiments. A pulse length of 1 μs was used in (a).

(b) the homonuclear (^{23}Na) 3Q MAS experiment in Fig. 1a, (c) a homonuclear (^{23}Na) 3Q MAS experiment based on that in Fig. 1a but with a 3Q inversion pulse, and (d) the heteronuclear (^{23}Na–^{1}H) MQ MAS experiment (with $\tau_{rcpl} = 1\ \tau_R$) in Fig. 1b. The MAS spectrum in Fig. 3a demonstrates clearly the difficulties presented by residual second-order quadrupolar broadening, since it is certainly not immediately evident that the observed spectrum is due to three crystallographically distinct sites. Comparing the MAS (Fig. 3a) and the 3Q MAS-filtered spectra (Fig. 3b), although the same features are present in both spectra, the broad features to the right of the two most intense sharp peaks (at the left) show a reduction in relative intensity in Fig. 3b. This illustrates a significant problem of the MQ MAS technique, namely the efficiency of MQ excitation as well as that of the subsequent conversion to observable SQC depend on the quadrupolar coupling (*65*), with a marked fall-off for sites with large C_Q values (the broad features on the right in the Na_2HPO_4 spectra are due to the Na(3) site, which has a C_Q value of 3.7 MHz). The development of methods which alleviate this problem has been and continues to be an area of active research; for example, Alemany *et al.* have recently shown that it is possible, using the DFS technique, to observe an ^{27}Al (spin $I = 5/2$) site with a C_Q of 18.5 MHz (*14*). Figure 3c shows that the incorporation of a 3Q inversion pulse leads to further spectral distortions as well as a factor of two loss in overall sensitivity. Such effects of a 3Q inversion pulse have been discussed previously in Ref. (*49*), where the results of computer simulations are also presented.

From the crystal structure data presented in Table 2, it is concluded that all three Na sites in Na_2HPO_4 have approximately the same proximity to two nearby protons. Thus, in this case, the recording of a heteronuclear (^{23}Na–^{1}H) MQ MAS-filtered spectrum should not lead to any spectral editing. Indeed, the spectrum in Fig. 3d is of a similar form to that in Fig. 3c, although the broad features due to the Na(3) site are lost in the noise. A fivefold reduction in sensitivity is observed as compared to the 3Q MAS experiment with a 3Q inversion pulse; it is to be noted that this reduction is in agreement with the relative intensities of the positive and negative peaks observed for the coherence counting experiment in Fig. 2b. As discussed below, the loss in sensitivity is largely due to homonuclear ^{1}H–^{1}H dipolar couplings acting during the finite ^{1}H π pulses. The poor sensitivity is a significant drawback of the heteronuclear MQ MAS experiment. However, the MQ MAS experiments incorporating CP (*38–46*) discussed in the Introduction also often suffer from poor sensitivity, since the advantage of the CP step arising from the difference in the magnetogyric ratios of the two nuclei is usually far outweighed by the proton having a significantly longer T_1 as compared to that of the quadrupolar nucleus. It is to be noted that Ashbrook and Wimperis recently presented an ^{17}O (at 35% isotopic enrichment) example where CP leads to a slight sensitivity enhancement, on account of the combination of the lower abundance and lower magnetogyric ratio of ^{17}O (as compared to, e.g., ^{23}Na) and the relatively large C_Q of the investigated site (*46*).

The optimum recycle delay in the heteronuclear MQ MAS experiment is the same as that in the 3Q MAS experiment, since both experiments begin with the excitation of spin-I 3QC. In this respect, it is significant to report that, in the course of this work, we noticed an interesting phenomenon, namely there was a difference in the optimum recycle delay for the simple MAS as compared to the 3Q MAS experiment. To determine the recycle delay which gives the optimum S/N, we adopted the procedure of doubling the recycle delay until the increase

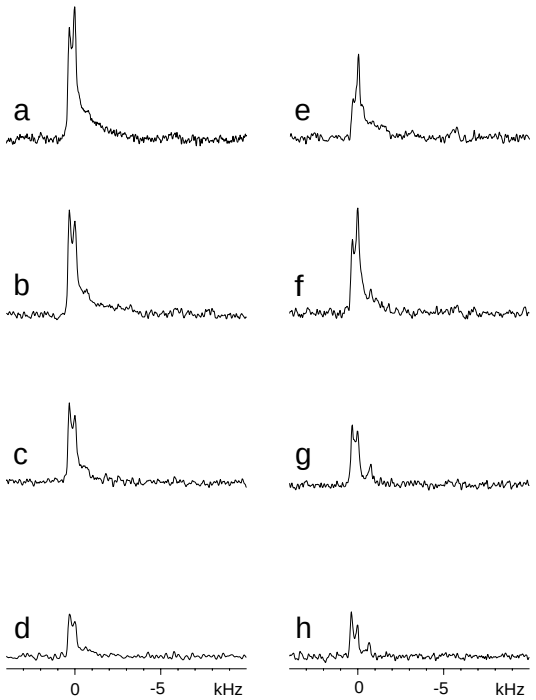

FIG. 4. MQ-filtered ($t_1 = 2\ \mu$s) spectra of Na_2HPO_4, recorded using the heteronuclear (^{23}Na–^{1}H) MQ MAS experiment in Fig. 1b at MAS frequencies of 10 kHz (a)–(d) and 20 kHz (e)–(h). Recoupling times of one (a, e), two (b, f), three (c, g), and four rotor periods (d, h) were used. In all experiments, 3744 transients were coadded and a recycle delay of 2 s was used.

in the signal intensity is less than a factor of $\sqrt{2}(=1.41)$. For ^{23}Na NMR of Na_2HPO_4, doubling the recycle delay from 1 to 2 s, from 2 to 4 s, and from 4 to 8 s gave increases in the signal intensity of 1.4, 1.3, and 1.2 for the one-pulse MAS experiment and 1.6, 1.6, and 1.3 for the 3Q MAS experiment. Thus, the optimum recycle delays are 2 and 4 s for the MAS and 3Q MAS experiments, respectively. (Note that different recycle delays were often used for the experimental spectra presented in this paper.)

Figure 4 presents MQ-filtered ($t_1 = 2\,\mu$s) spectra of Na_2HPO_4, recorded using the heteronuclear (^{23}Na–^{1}H) MQ MAS experiment in Fig. 1b. The spectra on the left- (Figs. 4a–4d) and right-hand (Figs. 4e–4h) sides were recorded at MAS frequencies of 10 and 20 kHz, respectively. On going from top to bottom, the recoupling time used increases from one to four rotor periods. In each case, the same recycle delay was used, and the same number of transients were co-added. The spectra are all plotted on the same vertical scale. It is then evident that, at MAS frequencies of 10 and 20 kHz, the maximum signal intensities are observed for $\tau_{rcpl} = 1\tau_R$ (Fig. 4a) and $2\ \tau_R$ (Fig. 4f), respectively. This observation is not surprising given that these cases correspond to the same recoupling time of 100 μs. Note also that similar lineshapes are observed when the recoupling time is the same, i.e., in Figs. 4a and 4f and 4b and 4h.

It is interesting to compare the sensitivity at the two MAS frequencies for the cases where τ_{rcpl} is the same. It is evident that the sensitivity is better at 10 kHz. This is due to, first, the dependence of 3Q excitation and conversion on ν_R (*84*). In this context, it is to be noted that Vosegaard *et al.* recently presented an approach, which, by employing rotary resonance excitation, allows efficient 3Q excitation and conversion at a high ν_R (*85*). In addition, at 20 kHz, there are more ^{1}H π pulses applied during the REDOR recoupling periods, as well as there being an increase in the proportion of a rotor period occupied by the π pulses. The greater importance of the latter effects is apparent from the significantly greater intensity difference between the spectra in Figs. 4b and 4h than that between those in Figs. 4a and 4f. This loss of sensitivity is a consequence of homonuclear ^{1}H–^{1}H dipolar couplings acting during the finite ^{1}H π pulses—such effects were previously observed by Chan and Eckert (*86*) and Saalwächter and Spiess (*29*). In the context of the analogous heteronuclear MQ MAS experiments for dipolar-coupled pairs of spin $I = 1/2$ nuclei, we note that such homonuclear dipolar effects at high ν_R are insignificant for pulse sequences, such as ^{1}H–^{13}C REPT (*27*, *28*, *33*) and inversely detected ^{1}H–^{15}N DIP-HSQC (*36*, *37*), where ^{1}H transverse magnetization evolves during the REDOR-recoupling periods, and the REDOR π pulses are applied on the ^{13}C or ^{15}N channel.

It is to be noted that Chan and Eckert (*86*) and Saalwächter and Spiess (*29*) propose an alternative REDOR reference experiment which compensates for the sensitivity losses due to homonuclear dipolar couplings. This method involves the application of an additional π pulse at the same time as the single π pulse on the other channel, such that the dipolar dephasings in the first and second halves become identical in magnitude but opposite in sign. For an isolated heteronuclear spin pair, there is hence no dephasing, as in a normal REDOR reference experiment where all the dephasing π pulses are simply omitted. Where homonuclear dipolar couplings are significant, the dephasing due to them during the π pulses is now also present in the alternative reference experiment, unlike the case of the normal reference experiment. Indeed, we recommend that such a reference experiment be employed in the 3Q-t_1-REDOR (*49*) and 3Q-t_2-REDOR (*48*) experiments.

In this section, we finally note that, for a sample where there is more than one distinct spin $I = 1/2$ resonance such that off-resonance effects will come into play, it is recommended to apply the xy-4 phase scheme (*87*) to the REDOR 180° pulses.

7. HETERONUCLEAR MQ MAS SPINNING-SIDEBAND PATTERNS: SIMULATED SPECTRA FOR AN ISOLATED SPIN PAIR

We now consider the role of the dipolar term, $S_D(t_1)$, in Eqs. [31] and [32]. Mathematically, as shown in the Appendix, the powder average of $S_D(t_1)$ over the φ angle can be expanded

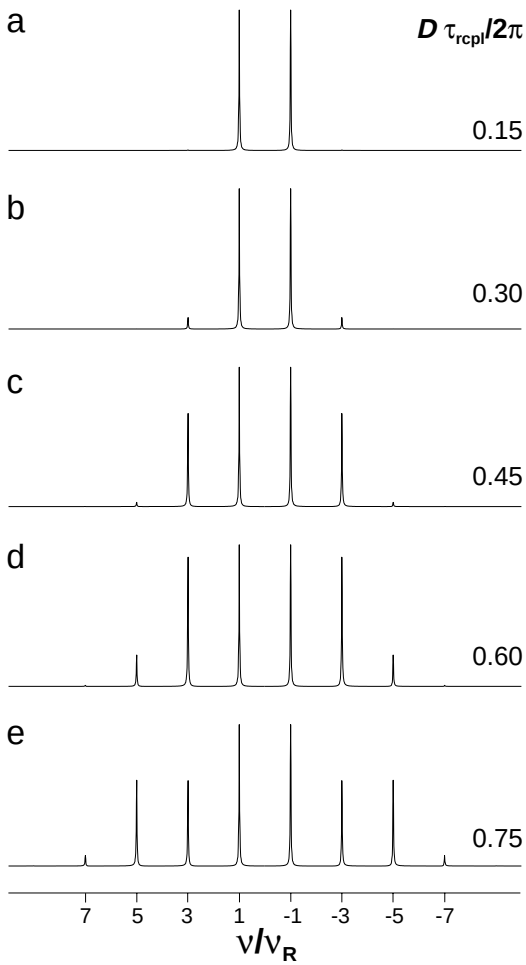

FIG. 5. Simulated heteronuclear MQ MAS spinning-sideband patterns for the ideal case of an isolated spin pair. The product of the dipolar coupling constant and the recoupling time, $D_{\mathrm{IS}}\,\tau_{\mathrm{rcpl}}/2\pi$, equals (a) 0.15, (b) 0.30, (c) 0.45, (d) 0.60, and (e) 0.75. Simulations were performed in the time domain by calculating numerically the powder average of the expression in Eq. [32].

as a series of Bessel functions:

$$\langle S_D(t_1)\rangle_\varphi = 2\sum_{n=0}^{+\infty}\left\{J_{2n+1}\left(\frac{6\sqrt{2}D_{IS}N\tau_R}{2\pi}\sin(2\theta)\right)\right\}^2 \times \cos\{(2n+1)\omega_R t_1\}. \quad [34]$$

The presence of only J_{2n+1} terms in Eq. [34] corresponds to the observation in the frequency domain of only odd-order spinning sidebands. The relative intensities of these spinning sidebands depend upon the product of the dipolar coupling constant and the recoupling time, $D_{\mathrm{IS}}\,\tau_{\mathrm{rcpl}}/2\pi$. This is illustrated by Fig. 5, which presents spectra corresponding to the Fourier transformation of FIDs simulated in the time domain by performing numerically the powder average of the expression in Eq. [32].

The origin of these unusual spinning-sideband patterns is well understood (*51–53*); whenever the efficiency of the reconversion of the state which is present during t_1 depends on the rotor phase angle, φ, the t_1-dependent change in φ at the start of the reconversion period relative to that at the start of the excitation period leads to the generation of a "rotor-encoded" spinning-sideband pattern, with the mechanism being referred to as reconversion rotor encoding (RRE) (*53*). For spin $I = 1/2$ nuclei, the marked sensitivity of the observed spinning-sideband patterns to the product of the dipolar coupling constant and the recoupling time (the latter is known and is under the control of the spectroscopist) has been exploited in both homonuclear ^{1}H DQ MAS (*16, 19*) and heteronuclear ^{1}H–^{13}C (*33*) and ^{1}H–^{15}N (*36*) MQ MAS experiments to probe dynamic processes and accurately measure internuclear distances.

It should be noted that the evolution of 3QC during the REDOR recoupling periods in the heteronuclear MQ MAS experiment of Fig. 1b leads to the presence of an additional factor of 3 for the $S_{\mathrm{D}}(t_1)$ term as compared to the corresponding expression for a MQ MAS experiment between a heteronuclear pair of spin $I = 1/2$ nuclei, where SQC evolves during the REDOR recoupling periods—compare Eq. [32] with Eqs. [4] and [6] of Ref. (*28*). For example, to generate the pattern in Fig. 5c, a $D_{\mathrm{IS}}\,\tau_{\mathrm{rcpl}}/2\pi$ value which is three times larger (1.35) would be required in the heteronuclear spin $I = 1/2$ experiment. Thus, the influence of the dipolar coupling can be considered to have been magnified by a factor of three by incorporating the evolution of 3QC. As compared to a homonuclear spin $I = 1/2$ experiment, the additional factor is reduced to 2, i.e., by a factor of 2/3, which reflects the difference between the homonuclear and heteronuclear dipolar Hamiltonians.

The simulated spectra presented in Fig. 5 correspond to purely dipolar rotor-encoded spectra. To investigate the additional influence of the $S_{\mathrm{Q}}(t_1,\ t_2)$ term and also to consider the importance of the finite lengths of both the spin-I and spin-S *rf* pulses, time-domain density matrix simulations were performed using the SIMPSON (*67*) NMR simulation program. (A representative SIMPSON input file is given in the Appendix.) It was found that the observed spinning-sideband patterns additionally depend on the quadrupolar parameters, i.e., C_{Q} and η, and the relative orientation of the dipolar and quadrupolar PASs, as well as the spin-I and spin-S 90° pulse lengths.

Figures 6 and 7 show, for example, the effect of changing the C_{Q} and the relative orientation of the dipolar and quadrupolar PASs, respectively. For all simulated spectra in Figs. 6 and 7, $D_{\mathrm{IS}}\,\tau_{\mathrm{rcpl}}/2\pi$ equals 0.75 (corresponding to the case in Fig. 5e), $\eta = 0$, and the spin-I and spin-S 90° pulse lengths equal 1.5 and 2.0 μs, respectively. Figure 6 illustrates that increasing C_{Q} leads to marked changes in the observed spinning-sideband pattern. For the relatively small value of $C_{\mathrm{Q}} = 1.0$ MHz in Fig. 6a, the pattern resembles that for the ideal dipolar only case in Fig. 5e, although, first, the third- and fifth-order sidebands have a weaker intensity relative to that of the first-order sidebands, and, second, weak centerband and even-order sideband intensity is observed. For the larger C_Q values, the odd-order spinning-sideband

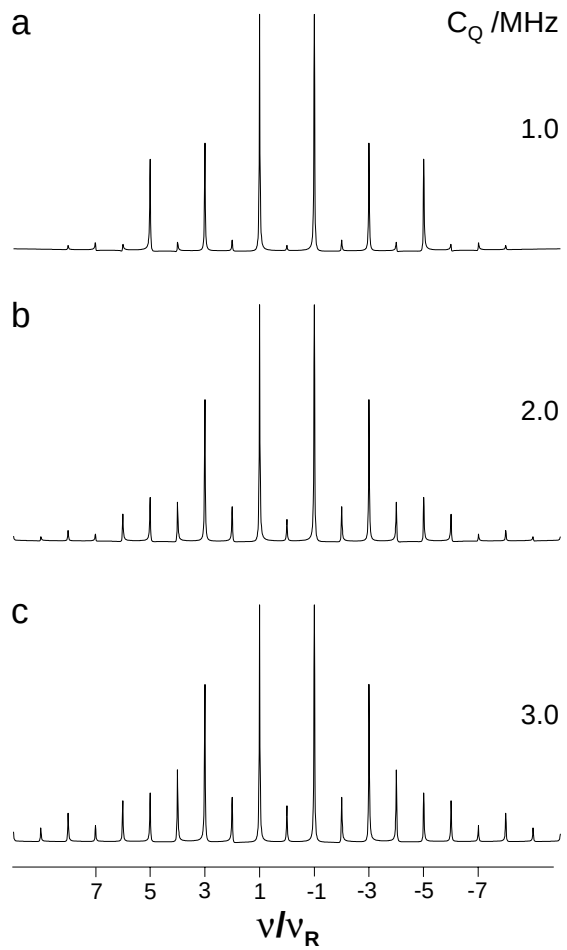

FIG. 6. The effect of changing C_Q upon the spinning-sideband patterns obtained using the heteronuclear MQ MAS experiment in Fig. 1b. C_Q equals (a) 1.0, (b) 2.0, and (c) 3.0 MHz. Density-matrix simulations were performed for an IS spin pair in the time domain using the SIMPSON (*67*) NMR simulation program. A representative SIMPSON input file is given in the Appendix. The following parameters were used: $D_{IS}/2\pi = 2.5$ kHz; $\eta = 0$; $\nu_R = 10$ kHz; $\tau_{rcpl} = 3\ \tau_R$; ^{1}H 90° pulse length = 2.0 μs; ^{23}Na 90° pulse length = 1.5 μs; ^{23}Na pulse lengths for 3Q excitation, 3Q inversion, and 3Q to 1Q conversion = 3.6, 3.0, and 1.5 μs, respectively. The quadrupolar and dipolar PASs were aligned with each other.

pattern changes noticeably, while the centerband and even-order sideband intensity increases appreciably. Figure 7 shows, for the case of $C_Q = 1.0$ MHz and $\eta = 0$, that changing the relative orientation of the dipolar PAS with respect to the quadrupolar PAS also leads to significant changes in the observed spinning-sideband pattern; for a perpendicular orientation (Fig. 7d), the third- and fifth-order spinning sidebands are both over 65% of the intensity of the first-order sidebands as compared to under 50% for a parallel orientation (Fig. 7a).

Experimental heteronuclear MQ MAS spinning-sideband patterns obtained using the pulse sequence in Fig. 1b, thus, depend on a number of both system and experimental parameters. However, the majority of these parameters are known in advance. In particular, a fitting of the anisotropically broadened lineshapes in a standard homonuclear MQ MAS experiment allows the determination of C_Q and η for each resolved site. The experimental 90° pulse lengths are also, of course, known—it is to be remembered, though, that the use of the correct experimental values in the simulations is essential in any fitting of experimental data. Considering the remaining parameters, namely the heteronuclear dipolar coupling and the relative orientation of the dipolar and quadrupolar PASs, the sideband patterns are more sensitive to the magnitude of the dipolar coupling, such that it should be possible to determine this to a good degree of accuracy.

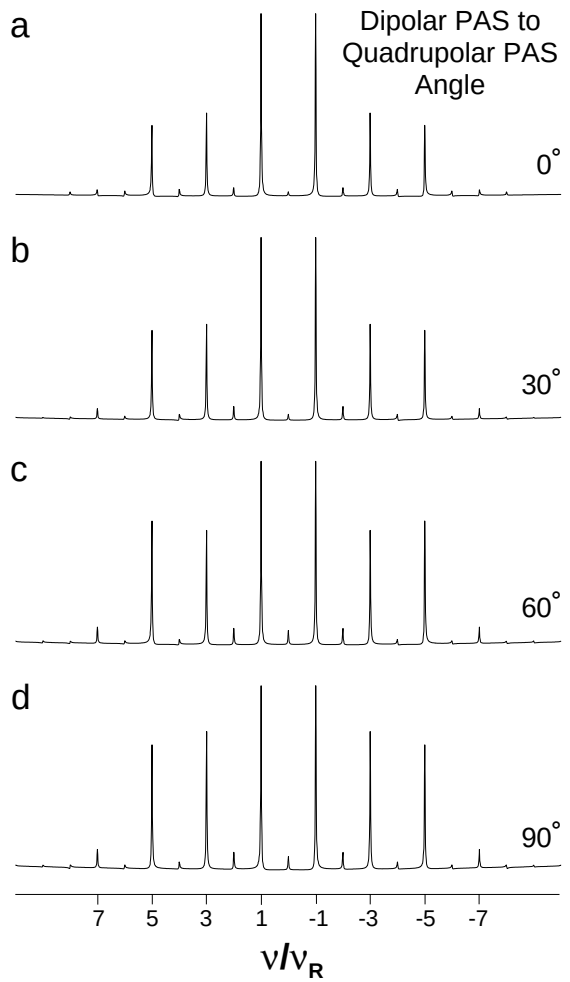

FIG. 7. The effect of changing the relative orientation of the quadrupolar and dipolar PASs upon the spinning-sideband patterns obtained using the heteronuclear MQ MAS experiment in Fig. 1b. The dipolar PAS is oriented at an angle of (a) 0°, (b) 30°, (c) 60°, and (d) 90° with respect to the quadrupolar PAS. Density-matrix simulations were performed for an IS spin pair in the time domain using the SIMPSON (*67*) NMR simulation program. A representative SIMPSON input file is given in the Appendix. The following parameters were used: $D_{IS}/2\pi = 2.5$ kHz; $C_Q = 1.0$ MHz; $\eta = 0$; $\nu_R = 10$ kHz; $\tau_{rcpl} = 3\ \tau_R$; ^{1}H 90° pulse length = 2.0 μs; ^{23}Na 90° pulse length = 1.5 μs; ^{23}Na pulse lengths for 3Q excitation, 3Q inversion, and 3Q to 1Q conversion = 3.6, 3.0, and 1.5 μs, respectively.

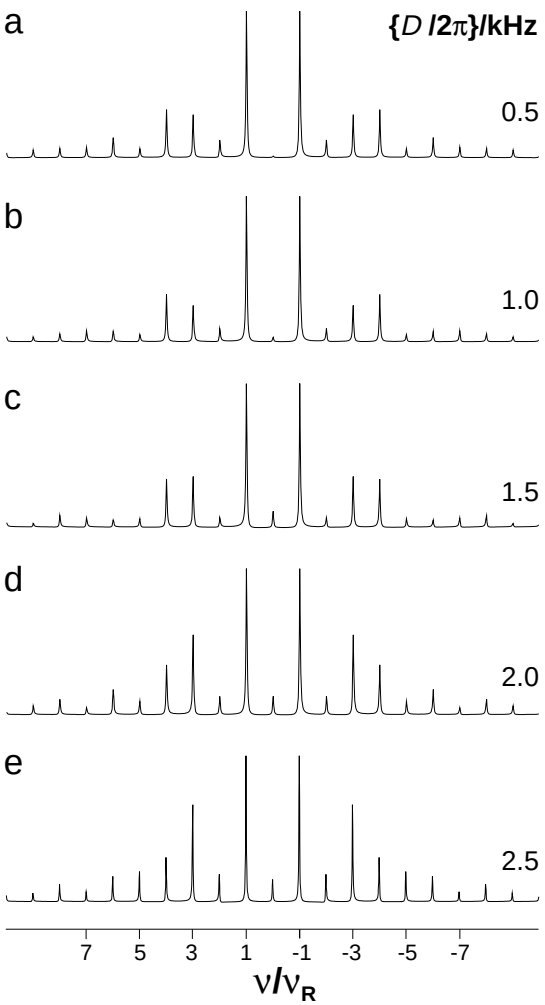

FIG. 8. The effect of changing the heteronuclear dipolar coupling upon the spinning-sideband patterns obtained using the heteronuclear MQ MAS experiment in Fig. 1b. $D_{IS}/2\pi$ equals (a) 0.5, (b) 1.0, (c) 1.5, (d) 2.0, and (e) 2.5 kHz. Density-matrix simulations were performed for an IS spin pair in the time domain using the SIMPSON (*67*) NMR simulation program. A representative SIMPSON input file is given in the Appendix. The following parameters were used: $C_Q = 1.0$ MHz; $\eta = 0$; $\nu_R = 10$ kHz; $\tau_{rcpl} = 3\,\tau_R$; ^{1}H 90° pulse length = 2.0 μs; ^{23}Na 90° pulse length = 1.5 μs; ^{23}Na pulse lengths for 3Q excitation, 3Q inversion, and 3Q to 1Q conversion = 3.6, 3.0, and 1.5 μs, respectively. The quadrupolar and dipolar PASs were aligned with each other.

In addition, it is to be noted that Pruski *et al.* have shown that the heteronuclear dipolar coupling can be reliably determined from a 3Q-t_1-REDOR build-up curve; simulations were presented which show that such build-up curves are relatively insensitive to C_Q, at least in the case of a high ν_{rf} (*49*). The combined application of the two methods would thus allow the determination of the relative orientation of the dipolar and quadrupolar PASs, since this would be the only free parameter in a fit of experimental heteronuclear MQ MAS spinning-sideband patterns.

Finally, it is to be emphasized that heteronuclear MQ MAS spinning-sideband patterns obtained using the pulse sequence in Fig. 1b show a marked sensitivity to both the heteronuclear dipolar coupling and the relative orientation of the dipolar and quadrupolar PASs, even for the case of a site with a large C_Q. This is illustrated by the simulated spectra in Figs. 8 and 9, which show the effect of changing the heteronuclear dipolar coupling constant and the relative orientation of the dipolar and quadrupolar PASs, respectively, for a C_Q of 3.0 MHz. In Fig. 8, it is evident that both the ratio of the intensities of the third- to first-, and fifth- to third-order spinning sidebands vary noticeably on increasing D_{IS}. Moreover, Fig. 9 shows that the intensities of the higher order odd spinning sidebands relative to that of the

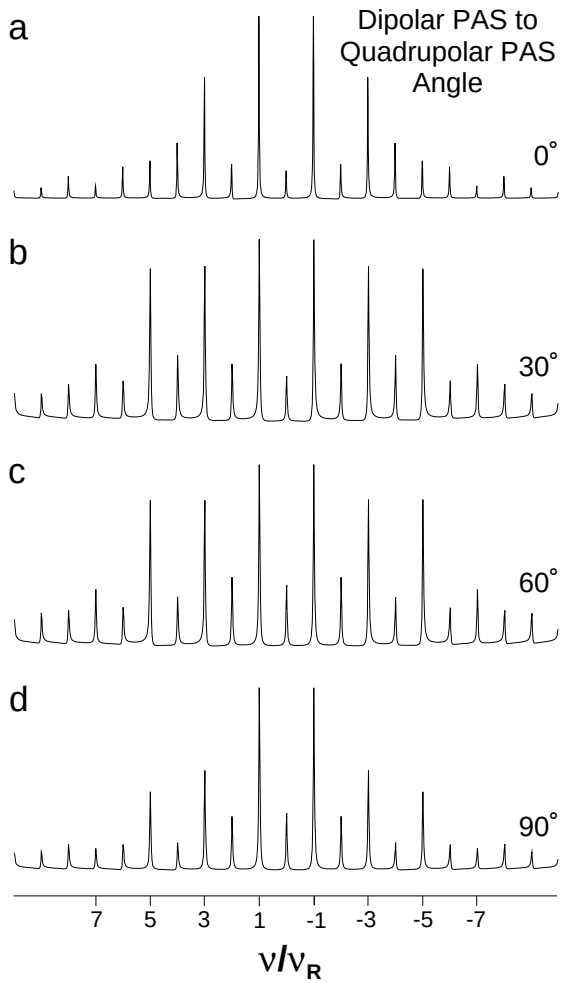

FIG. 9. The effect of changing the relative orientation of the quadrupolar and dipolar PASs upon the spinning-sideband patterns obtained using the heteronuclear MQ MAS experiment in Fig. 1b. The dipolar PAS is oriented at an angle of (a) 0°, (b) 30°, (c) 60°, and (d) 90° with respect to the quadrupolar PAS. Density-matrix simulations were performed for an IS spin pair in the time domain using the SIMPSON (*67*) NMR simulation program. A representative SIMPSON input file is given in the Appendix. The following parameters were used: $D_{IS}/2\pi = 2.5$ kHz; $C_Q = 3.0$ MHz; $\eta = 0$; $\nu_R = 10$ kHz; $\tau_{rcpl} = 3\,\tau_R$; ^{1}H 90° pulse length = 2.0 μs; ^{23}Na 90° pulse length = 1.5 μs; ^{23}Na pulse lengths for 3Q excitation, 3Q inversion, and 3Q to 1Q conversion = 3.6, 3.0, and 1.5 μs, respectively.

first-order ones are significantly different for different orientations of the two PASs.

8. SPINNING-SIDEBAND PATTERNS IN THE MQ MAS EXPERIMENT

Figure 10 presents two-dimensional spectra recorded for Na_2HPO_4 using (a) the homonuclear (^{23}Na) 3Q MAS and (b) the heteronuclear (^{23}Na–^{1}H) MQ MAS pulse sequences in Figs. 1a and 1b, respectively. For both spectra, after Fourier transformation in both dimensions, a shearing transformation was applied such that the anisotropically broadened ridges lie parallel to the SQ (F_2) axis. In this way, the shown F_1 (skyline) projections correspond to the isotropic dimension, in which the residual second-order quadrupolar broadening has been removed. At a ^{23}Na Larmor frequency of 132.5 MHz, the Na(1) and Na(2) sites in Na_2HPO_4 are only just resolved in the 3Q MAS experiment; the Na(2) site has the smaller C_Q and corresponds to the most intense peak in the isotropic projection. The long anisotropically broadened ridge due to the high-C_Q Na(3) site can be clearly identified in the centre of Fig. 10a (it is also evident, though with a weak intensity, in Fig. 10b).

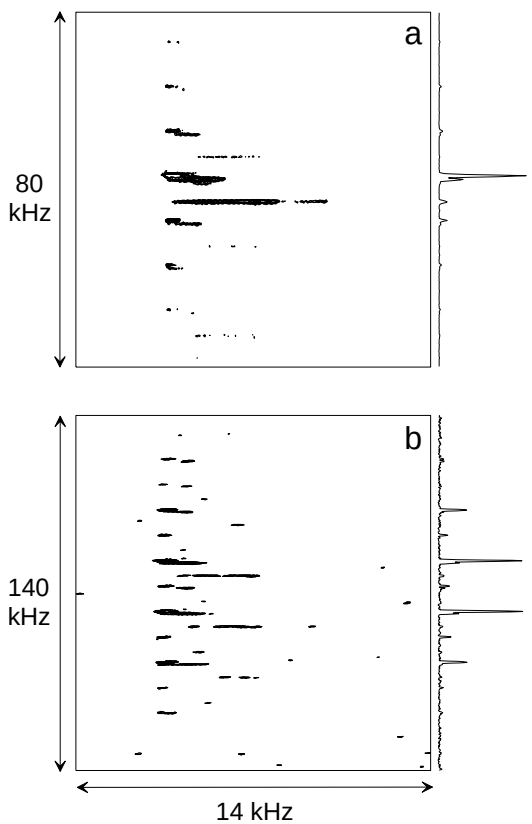

FIG. 10. Two-dimensional spectra recorded for Na_2HPO_4 using (a) the homonuclear (^{23}Na) 3Q MAS and (b) the heteronuclear (^{23}Na–^{1}H) MQ MAS (with $\tau_{rcpl} = 2\ \tau_R$, and a ^{1}H spin lock during t_1) pulse sequences in Figs. 1a and 1b, respectively. The MAS frequency was 10 kHz. After Fourier transformation in both dimensions, a shearing transformation was applied such that the anisotropically broadened ridges lie parallel to the SQ (F_2) axis. Skyline projections are shown for the MQ (F_1) dimension. In (a) and (b), respectively, 48 and 288 transients were coadded for each of 370 and 370 t_1 points, with a t_1 increment of 6.0 and 3.5 μs and a recycle delay of 2.0 and 1.4 s. In both cases, sign discrimination was restored in the F_1 dimension for the ^{23}Na resonances by the TPPI (*99*) method, which involves incrementing the phase(s) of the ^{23}Na pulse(s) applied before t_1 by 30° after recording each t_1 point. The bottom contour level corresponds to 1 and 8% of the maximum intensity in (a) and (b), respectively.

Spinning-sidebands are observed in both Figs. 10a and 10b. However, the sideband patterns are very different. In the (^{23}Na) 3Q MAS spectrum (Fig. 10a), the signal is concentrated at the centerband position. By comparison, in the heteronuclear (^{23}Na–^{1}H) MQ MAS spectrum (Fig. 10b), as predicted in the previous section, the centerband and even-order sideband intensities are weak, with intense signal being observed at the first- and third-order sideband positions. These experimental heteronuclear MQ MAS spinning-sideband patterns will be discussed below in Section 10; in this section, we consider first the origin of the homonuclear 3Q MAS spinning-sideband patterns. For the Na(2) site, a lineshape analysis of the sideband pattern in Fig. 10a reveals that the -1 and $+1$ sidebands have integrated intensities of 11 and 7% of that of the centerband.

An inspection of the literature reveals different explanations for the origin of homonuclear 3Q MAS spinning-sideband patterns. In Ref. (*88*), Marinelli and Frydman present simulations which show that the experimentally observed MQ MAS spinning-sideband patterns can be explained by a rotor encoding, of the type discussed in the previous section, of the quadrupolar interaction. Support for this mechanism is provided by Amoureux *et al.* who present both experimental and simulated MQ MAS spinning-sideband patterns, where the observed patterns vary upon changing the pulse lengths (*84*). Charpentier *et al.* have further presented simulations based on a Floquet formalism which support the conclusions reached by Marinelli and Frydman (*89*). By comparison, according to Duer, it is necessary to include both homonuclear dipolar couplings as well as the CSA to explain an experimental 3Q MAS spectrum (*90*). Finally, Wang *et al.* have shown that the isotropic 3Q MAS ^{87}Rb spectrum of Rb_2CrO_4 can be well fit in terms of the CSA alone (*91*), although it is to be noted that the CSA ($\delta = -110$ ppm) is very large for this sample.

Simulated 3Q MAS spinning-sideband patterns for an isolated spin $I = 3/2$ nucleus are presented in Fig. 11; simulations were carried out using the SIMPSON (*67*) NMR simulation program. (A representative SIMPSON input file is again given in the Appendix.) In each case, the spectra are dominated by an intense centerband; since it is the spinning sidebands which are of interest, the centerband has been truncated at 25% of its full height. The simulations mimic the experimental parameters used to record the 3Q MAS spectrum in Fig. 10a, and quadrupolar parameters corresponding to those of the Na(2) site in Na_2HPO_4 were used. The simulated spectrum in Fig. 11a corresponds to a consideration of solely the first-order quadrupolar interaction, while, in Figs. 11b–11e, a CSA is additionally

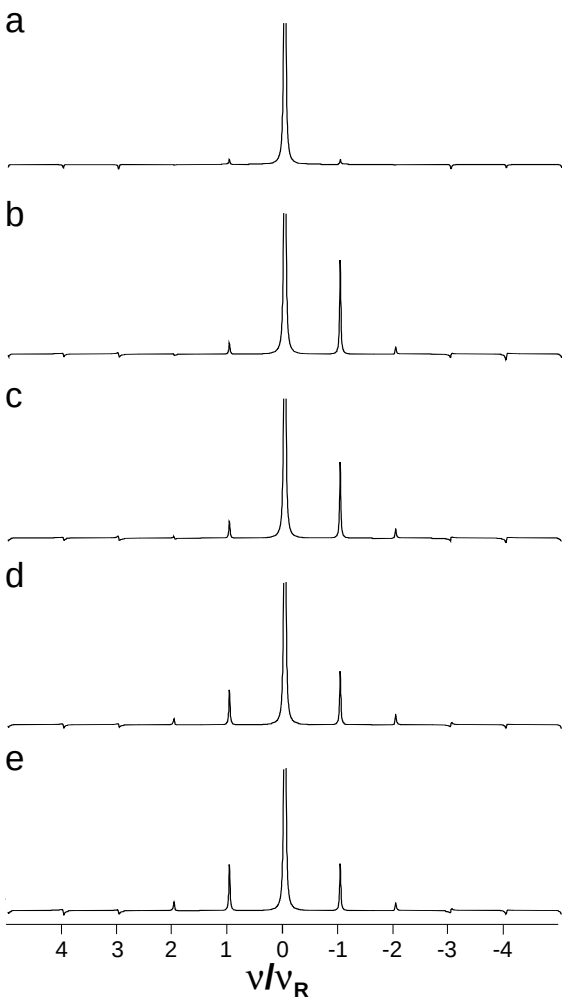

FIG. 11. An investigation of the origin of homonuclear 3Q MAS spinning-sideband patterns. The simulated spectrum in (a) corresponds to a consideration of solely the quadrupolar interaction, while, in (b)–(e), a CSA ($\delta = 3.0$ kHz, $\eta = 0$) is additionally included. The z axis of the CSA PAS is oriented at an angle of (b) 0°, (c) 30°, (d) 60°, and (e) 90° with respect to that of the quadrupolar PAS. In each spectrum, the centerband has been truncated at 25% of its full height. Density-matrix simulations were performed for an isolated spin $I = 3/2$ nucleus in the time domain using the SIMPSON (*67*) NMR simulation program. A representative SIMPSON input file is given in the Appendix. The following parameters were used: $C_Q = 1.4$ MHz; $\eta = 0.2$; $\nu_R = 10$ kHz; ^{23}Na 90° pulse length = 1.75 μs; ^{23}Na pulse lengths for 3Q excitation and 3Q to 1Q conversion = 3.5 and 1.75 μs, respectively.

included, with the effect of changing the relative orientation of the CSA PAS with respect to the quadrupolar PAS being investigated.

In Fig. 11a, it is evident that only very weak spinning sidebands are observed—the maximum intensity is only about 1% of the centerband. It is, though, to be noted that, first, the C_Q of the Na(2) site is small and, second, a high ^{23}Na rf field strength was employed such that the ^{23}Na pulse lengths are short. Indeed, other simulated spectra (not shown) demonstrated that more intense spinning-sidebands, i.e., the intensities are of the order of 5% or more of that of the centerband, are observed for conditions which favor the rotor-encoding mechanism, namely higher C_Q values and longer ^{23}Na pulse lengths. However, we observed that the rotor encoding of the *first-order* quadrupolar interaction always leads to *symmetric* sideband patterns.

Upon solely additionally including the CSA in the simulations, it proved possible to reproduce the experimental spinning-sideband pattern for the Na(2) site in Fig. 10a. The simulated spectrum in Fig. 11b corresponds to CSA parameters of $\delta =$ 3.0 kHz (for a ^{23}Na Larmor frequency of 132.3 MHz, i.e., corresponding to 22.7 ppm) and $\eta = 0$, with the CSA and quadrupolar PASs aligned. Other simulations (not shown) demonstrate that the first-order sideband intensities grow as the CSA δ is increased from 0 to 4 kHz. Figures 11b–11e show that changing the orientation of the CSA PAS with respect to the quadrupolar PAS leads to a change from a marked asymmetry when the two PASs are aligned to an almost symmetric pattern for a perpendicular arrangement.

Two potential mechanisms leading to the generation of the observed spinning-sideband patterns in Figs. 11b–11e can be identified, namely, first, the simple evolution during t_1 of ^{23}Na 3QC under the CSA, and, second, the reconversion rotor encoding of the ^{23}Na CSA. Within the framework of the SIMPSON (*67*) NMR simulation program, it is straightforward to "turn off" evolution under the ^{23}Na CSA. In this case, a simulation corresponding to that in Fig. 11b yielded a spectrum (not shown) in which the intensities of the sidebands are reduced to 1% of that of the centerband. It is, thus, evident that evolution during t_1 is essential for the generation of CSA-dependent spinning-sideband patterns. Does this mean that the rotor-encoding mechanism plays no role? In this context, it is interesting to consider the effect of changing the CSA η from 0 to 1 (spectra not shown); for the case of the CSA and quadrupolar PASs being aligned (i.e., equivalent to Fig. 11b), a marked asymmetry of the first-order sidebands was found to remain (the -1 sideband intensity is over twice that of the $+1$ sideband). This is to be contrasted to a standard one-pulse (SQ) experiment, where a CSA tensor with $\eta = 1$ gives a symmetric sideband pattern. Moreover, a simulation, which artificially started with a spin $I = 3/2$ 3QC state and used a 3QC detection operator, for the same conditions as in Fig. 11b except that the CSA η was set equal to 1 gave a symmetric spinning-sideband pattern. Thus, it is evident that an interplay of the CSA and quadrupolar interactions and the rf irradiation during the excitation and conversion pulses does plays a role in determining the observed 3Q MAS spectrum.

This section has shown that the spinning-sideband patterns observed in homonuclear 3Q MAS spectra are sensitive to the CSA. By varying the anisotropy, asymmetry, and orientation of the CSA, we found that the experimentally observed 3Q MAS spectrum (Fig. 10a) for the Na(2) site in Na_2HPO_4 was reproduced using the following parameters: $\delta = 2.8$ kHz, $\eta = 1$, and an angle of 30° between the z axes of the CSA and quadrupolar PASs. The value of $\delta = 2.8$ kHz (which corresponds to 21 ppm)

is of the same order of magnitude as that determined for the ^{23}Na CSA in a crown ether complex, $Na(12C4)_2ClO_4$, by Wong and Wu (*92*). In this latter study, an analysis of the static ^{23}Na spectrum revealed that the CSA contribution to the powder lineshape (also at a ^{23}Na Larmor frequency of 132.3 MHz) is 1.8 kHz.

For the Na(2) site in Na_2HPO_4, the second-order quadrupolar broadening is small. To conclude this section, it is necessary to consider the situation, frequently encountered in applications of the MQ MAS method, where the C_Q values are larger. In such cases, in direct analogy to the above discussion of the CSA, it is to be expected that evolution under the *second-order* quadrupolar broadening during t_1 leads to the generation of *asymmetric* spinning-sideband patterns. Since the quadrupolar parameters can be straightforwardly determined, it is possible, though, to determine, by means of simulated spectra, whether an additional mechanism, e.g., the CSA, is required to explain the experimental sideband pattern, as is the case for the Na(2) site in Na_2HPO_4. It is to be remembered that the CSA will become increasingly important at higher B_0 fields. Finally, it is to be noted that heteronuclear dipolar couplings can also (if heteronuclear decoupling is not employed) lead to sideband intensity; however, in this case, symmetric sideband patterns are always observed.

9. THE HETERONUCLEAR MQ MAS EXPERIMENT: THE CONTRIBUTION OF HOMONUCLEAR PROTON DIPOLAR COUPLINGS TO RELAXATION DURING t_1

In this section, we consider the role of homonuclear proton–proton dipolar couplings upon the evolution during t_1 of the mixed coherence state in the heteronuclear MQ MAS experiment. Figure 12 compares MQ (t_1) FIDs recorded for Na_2HPO_4 using (a) the homonuclear (^{23}Na) 3Q MAS and (b)–(d) the heteronuclear (^{23}Na–^{1}H) MQ MAS pulse sequences in Figs. 1a and 1b, respectively. The MAS frequency was 10 kHz in Figs. 12a–12c and 30 kHz in (Fig. 12d). In (Fig. 12c), a spin lock, i.e., a continuous pulse with its phase aligned along the direction of the transverse magnetization, was applied on the ^{1}H channel during t_1; this has the effect of reducing the homonuclear ^{1}H dipolar couplings by a factor of minus two (*1*, *93*). Comparing Figs. 12b and 12c, the extension of the FID, which results as a consequence of the reduction of relaxation due to homonuclear proton dipolar couplings is evident.

The corresponding resolution enhancement in the frequency domain yielded by a spin lock is illustrated in Fig. 13, which presents MQ spinning-sideband patterns obtained for Na_2HPO_4 using the heteronuclear (^{23}Na–^{1}H) MQ MAS pulse sequence in Fig. 1b, with a MAS frequency of 10 kHz and $\tau_{rcpl} = 1\ \tau_R$. A ^{1}H spin lock was applied during t_1 in (b). The presented spectra correspond to a summation over the F_2 spectral range due to the Na(2) site for sheared two-dimensional spectra. It is to be noted that the resolution enhancement in Fig. 13b is not simply due to the use of a longer t_1^{max} value; a better resolution

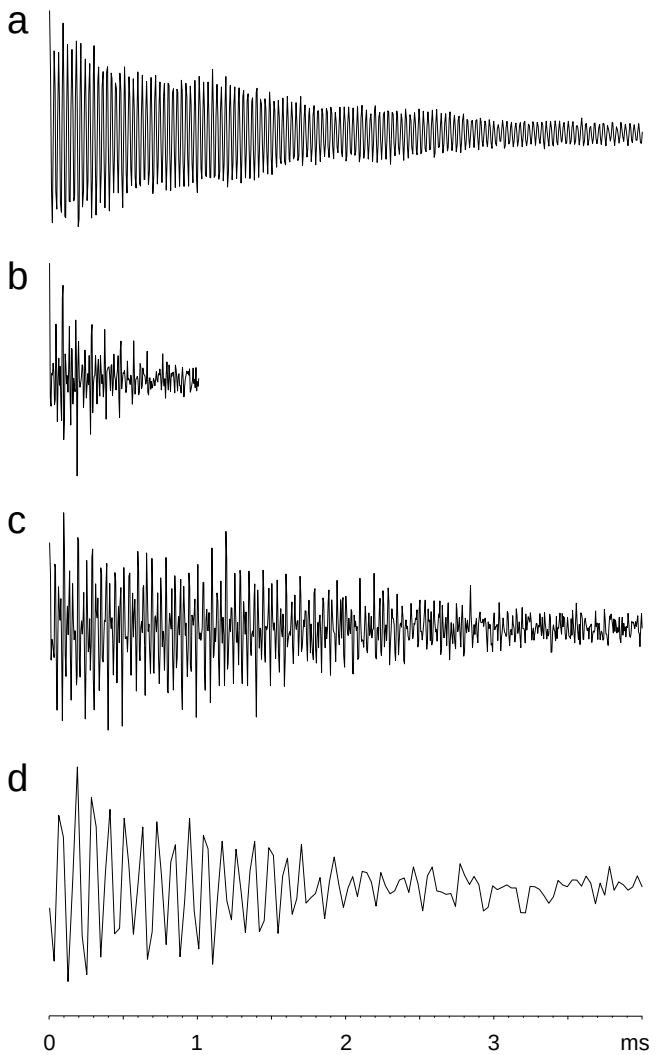

FIG. 12. MQ (t_1) FIDs recorded for Na_2HPO_4 using (a) the homonuclear (^{23}Na) 3Q MAS and (b)–(d) the heteronuclear (^{23}Na–^{1}H) MQ MAS pulse sequences in Figs. 1a and 1b, respectively. The MAS frequency was 10 kHz in (a)–(c) and 30 kHz in (d). Recoupling times of one (b, c), and two (d) rotor periods were used. In (c), a ^{1}H spin lock was applied during t_1.

than that in Fig. 13a was obtained (spectrum not shown) for the case where the experimental time-domain data set giving rise to the spectrum in Fig. 13b was truncated to the shorter t_1^{max} value.

The spin lock additionally achieves heteronuclear decoupling; the removal of evolution during t_1 under perturbing heteronuclear dipolar couplings, i.e., a coupling of ^{23}Na to a proton external to the heteronuclear MQC (remember that each ^{23}Na nucleus has two approximately equidistant proton neighbors), is evidenced by the lower centerband and even-order sideband intensity in Fig. 13b. The generation of such spinning sidebands by the influence of a perturbing coupling because of what is termed the evolution rotor modulation mechanism is discussed

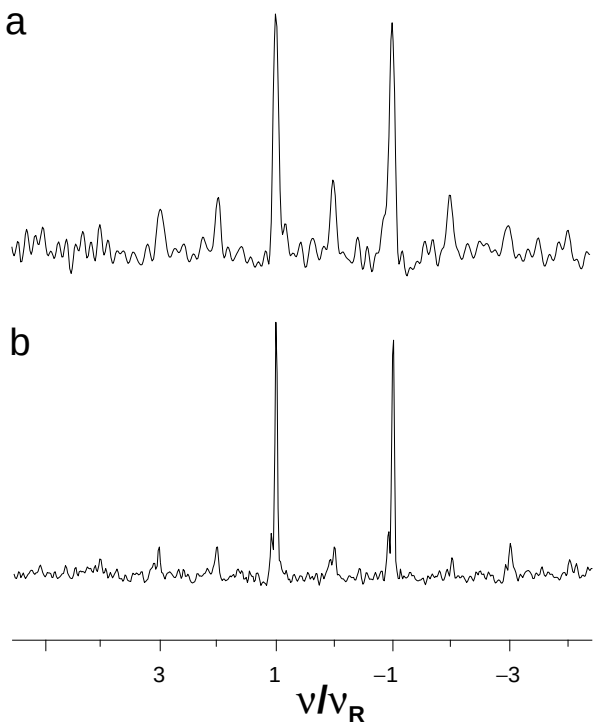

FIG. 13. MQ spinning-sideband patterns obtained for Na_2HPO_4 using the heteronuclear (^{23}Na–^{1}H) MQ MAS pulse sequence in Fig. 1b, with a MAS frequency of 10 kHz and $\tau_{rcpl} = 1\ \tau_R$. A ^{1}H spin lock was applied during t_1 in (b). The presented spectra correspond to a summation over the F_2 spectral range due to the Na(2) site for sheared two-dimensional spectra. Sign discrimination was restored in the F_1 dimension for the ^{23}Na resonances by the TPPI (*99*) method, which involves incrementing the phases of the ^{23}Na pulses applied before t_1 by 30° after recording each t_1 point. For each of 211 and 362 t_1 points in (a) and (b), respectively, 288 transients were coadded with a t_1 increment of 5.0 μs and a recycle delay of 1.4 s.

in Ref. (*53*). This mechanism could be investigated by means of a related experiment in which the two ^{1}H 90° pulses, which bracket t_1 in Fig. 1b, are brought together. In this way, they simply act as a MQ-filter, such that heteronuclear (^{23}Na) 3QC evolves during t_1. Since the proton magnetization is in a longitudinal rather than a transverse state, there is no signal loss due to dephasing because of homonuclear proton dipolar couplings. However, heteronuclear dipolar couplings to protons external to the heteronuclear 3QC remain active.

Another means by which homonuclear dipolar couplings can be decreased is to increase the MAS frequency; as shown in Fig. 12d, the MQ FID obtained for a heteronuclear MQ MAS experiment at $\nu_R = 30$ kHz (without a ^{1}H spin lock) is significantly longer compared to that (Fig. 12b) recorded at $\nu_R = 10$ kHz. However, as discussed in Section 6, the sensitivity of a heteronuclear MQ MAS experiment (for a constant τ_{rcpl}) falls off with increasing ν_R. For example, we were not able to record a spinning-sideband pattern with a reasonable sensitivity at $\nu_R = 30$ kHz showing third-order spinning sidebands. Instead, the experimental sideband patterns which are presented in the following section were recorded at $\nu_R = 10$ kHz using a ^{1}H spin-lock during t_1.

A spin lock (or the heteronuclear 3QC experiment), of course, has the significant disadvantage of causing the loss of ^{1}H chemical shift information. For Na_2HPO_4, as noted in Section 2, only a single hydrogen-bonded peak is observed in the ^{1}H spectrum, and, thus, the ^{1}H chemical shift information is not relevant in this case. An alternative approach, which was not pursued in this study, would be the application of a "windowless" homonuclear decoupling sequence during t_1. Specific examples are the Lee–Goldburg (LG) technique (*94*) and refinements, namely the frequency-switched and phase-modulated LG (FSLG (*30, 95*) and PMLG (*96*) sequences, as well as the computer-optimized sequence, DUMBO-1 (*97*). These sequences function well at a ν_R between 10 and 15 kHz.

10. HETERONUCLEAR MQ MAS SPINNING-SIDEBAND PATTERNS: EXPERIMENTAL SPECTRA FOR THE H-Na-H SYSTEM IN Na_2HPO_4

Figure 14 presents the sum projection, over the F_2 spectral range corresponding to the central-transition lineshapes of the three Na sites, for the two-dimensional heteronuclear (^{23}Na–^{1}H) MQ MAS spectrum of Na_2HPO_4 presented in Fig. 10b. The positions of the spinning sidebands within the sideband manifolds of the three Na sites are labeled separately. Comparing the three different spinning-sideband patterns, it is apparent that the intensities of the centerband and even-order sidebands relative to those of the odd-order sidebands are significantly larger for the Na(3) site, as compared to the case of the Na(1) and Na(2) sites. Recalling the simulated spectra presented in Fig. 6, this observation can be understood by remembering (see Table 1) that the Na(3) site has a significantly larger C_Q (3.7 MHz).

A detailed investigation of the structure of Na_2HPO_4 is not a primary aim of this work, rather the primary aim is to present the new NMR method. Therefore, in the following, only the spinning-sideband patterns due to the Na(2) site are analyzed. It is, however, to be emphasized that this focusing on the site with the lowest C_Q does not imply that it is not possible to extract structural parameters from heteronuclear MQ MAS spinning-sideband patterns due to sites with medium and large C_Q values. Indeed, the simulated sideband patterns for an isolated spin pair in Figs. 8 and 9 (Section 7) demonstrated that a marked sensitivity to both the heteronuclear dipolar coupling and the relative orientation of the dipolar and quadrupolar PASs is observed for a large C_Q value of 3.0 MHz. As in a standard (homonuclear) MQ MAS spectrum, it is to be noted, though, that the sensitivity is better for the Na(2) sidebands in Fig. 14 on account of the narrow second-order quadrupolar broadened pattern and the good MQ excitation and reconversion efficiency.

Figure 15 presents MQ spinning-sideband patterns obtained for Na_2HPO_4 using the heteronuclear (^{23}Na–^{1}H) MQ MAS pulse sequence in Fig. 1b. The presented spectra correspond to a summation over the F_2 spectral range due to the Na(2) site for sheared

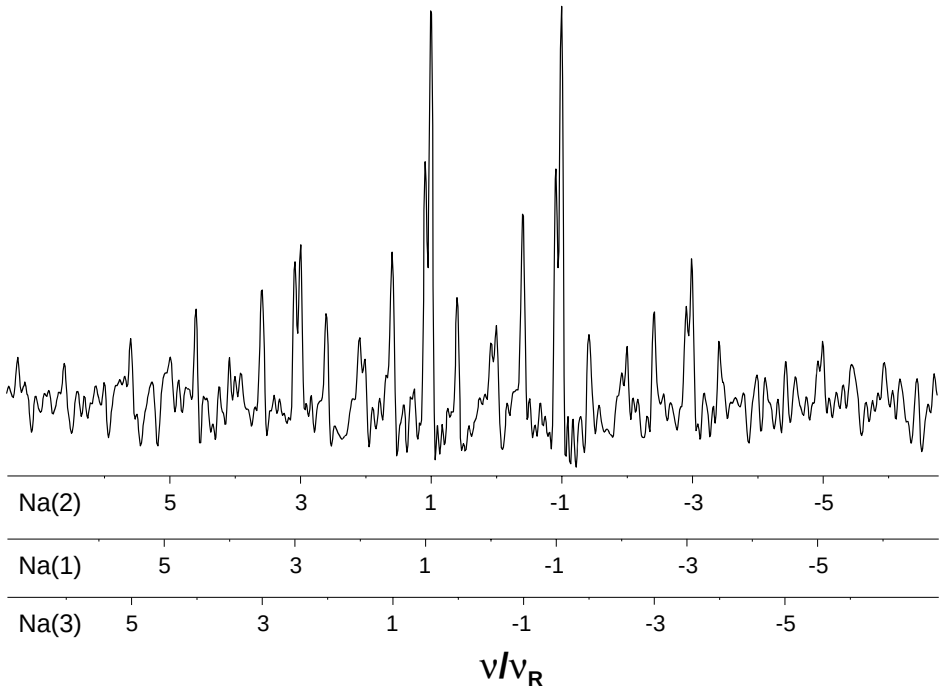

FIG. 14. The sum projection, over the F_2 spectral range corresponding to the central-transition lineshapes of the three Na sites, for the two-dimensional heteronuclear (^{23}Na–^{1}H) MQ MAS spectrum ($\tau_{rcpl} = 2\ \tau_R$, $\nu_R = 10$ kHz, a ^{1}H spin lock was applied during t_1) of Na_2HPO_4 presented in Fig. 10b. The positions of the spinning sidebands within the sideband manifolds of the three Na sites are labeled separately.

two-dimensional spectra. A ^{1}H spinlock was applied during t_1 and $\nu_R = 10$ kHz. The three patterns correspond to recoupling times of (Fig. 15a) one, (15b) two, and (15c) three rotor periods; the patterns are dominated by odd-order sideband intensity, with the intensities of the higher order spinning sidebands increasing as τ_{rcpl} increases. The contribution of the Na(1) site is evident for the lower order spinning sidebands as a small shoulder on the left-hand side. The integrated relative sideband intensities for the odd-order sidebands due to the Na(2) site, as obtained by means of lineshape analyses, are given in Table 4.

In the following, the quantitative determination of structural information from the experimental spinning-sideband patterns in Fig. 15 is considered. First, it is to be recalled that the simulations in Section 7 for an isolated spin pair have demonstrated a dependence of the observed spinning-sideband patterns on the heteronuclear dipolar coupling, the quadrupolar parameters (C_Q and η), the relative orientation of the dipolar and quadrupolar PASs, and the spin-I and spin-S 90° pulse lengths. Some simplification of the situation is immediately possible since the quadrupolar parameters, C_Q and η (see Table 1), and the experimental 90° pulse lengths are not free parameters; their known values were used in all the simulations described below.

TABLE 4

Relative Sideband Intensities[a] for the Na(2) Site in the Heteronuclear MQ MAS Spinning-Sideband Patterns in Fig. 15

τ_{rcpl}/τ_R	3rd/1st	5th/1st
1	0.11	—
2	0.32	0.08
3	0.29	0.21

[a] An average for the $+n$ and $-n$ sidebands is considered.

If no additional information, e.g., diffraction data, is available, the next step would be a fit of the experimental spinning-sideband patterns to simulated spectra for which both the heteronuclear dipolar coupling and the relative orientation of the dipolar and quadrupolar PASs were varied. Adopting such an approach here, it was found that it was not possible to simulate, for the case of an isolated spin pair, spinning-sideband patterns in agreement with the experimental data in Fig. 15. For Na_2HPO_4, additional information in terms of a refined crystal structure (*63*) is available; as stated in Section 2 (see Table 2), for the Na(2) site, there are, according to the crystal structure, two equidistant (0.270 nm) protons, with the H–Na–H vector being linear. It is, thus, unsurprising that simulated two-spin spectra cannot reproduce the experimental data. The following question must now be addressed: is it possible to extract structural information from heteronuclear MQ MAS spinning-sideband patterns for the more complicated case of a three-spin H–Na–H system?

It is straightforward to extend the analytical description of the heteronuclear MQ MAS experiment presented in Section 4 to include a heteronuclear dipolar coupling of the spin $I = 3/2$ nucleus to a second spin $I = 1/2$ nucleus. Since the corresponding

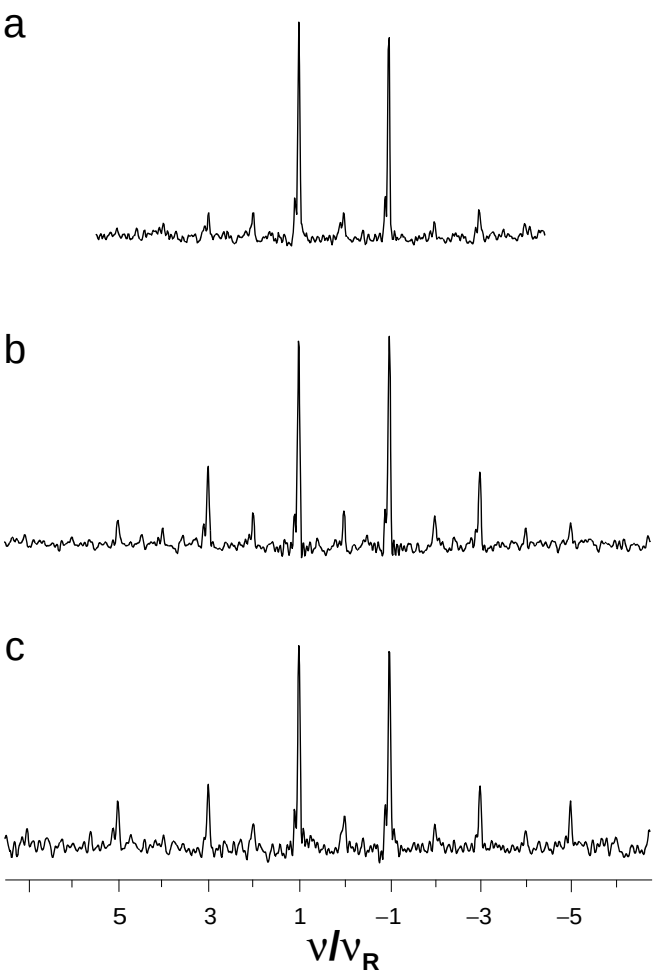

FIG. 15. MQ spinning-sideband patterns obtained for Na_2HPO_4 using the heteronuclear (^{23}Na–^{1}H) MQ MAS (with a ^{1}H spinlock during t_1) pulse sequence in Fig. 1b. The MAS frequency was 10 kHz, and the recoupling times were (a) one, (b) two, and (c) three rotor periods. The presented spectra correspond to a summation over the F_2 spectral range due to the Na(2) site for sheared two-dimensional spectra. Sign discrimination was restored in the F_1 dimension for the ^{23}Na resonances by the TPPI (*99*) method, which involves incrementing the phases of the ^{23}Na pulses applied before t_1 by 30° after recording each t_1 point. In (a), (b), and (c), respectively, 288, 288, and 288 transients were coadded for each of 362, 370, and 364 t_1 points, with a t_1 increment of 5.0, 3.5, and 3.5 μs and a recycle delay of 1.4, 1.4, and 1.3 s.

Hamiltonians commute, the evolution under the two heteronuclear dipolar couplings can be considered sequentially. The experimental use of phase cycling to select *S*-spin SQC during t_1 corresponds to selecting, at the end of the first REDOR recoupling period, only the $|\pm 3/2\rangle\langle\mp 3/2|S_z$ state. Making use of Eq. [30] and making the assumption that there is no evolution under the heteronuclear dipolar coupling during t_1 (this is valid for the case of the application of a ^{1}H spin lock), the total time-domain signal for an IS_2 system is, thus, given by

$$S(t_1, t_2) = \left\{S_D^I(t_1) + S_D^{II}(t_1)\right\} S_Q(t_1, t_2), \qquad [35]$$

where

$$\begin{aligned} S_D^I(t_1) = {} & \sin\left\{6N\Omega_D^I(\tau_R/2, 0)\right\} \cos\left\{6N\Omega_D^{II}(\tau_R/2, 0)\right\} \\ & \times \sin\left\{6N\Omega_D^I(\tau_R/2 + t_1, t_1)\right\} \\ & \times \cos\left\{6N\Omega_D^{II}(\tau_R/2 + t_1, t_1)\right\} \\ S_D^{II}(t_1) = {} & \sin\left\{6N\Omega_D^{II}(\tau_R/2, 0)\right\} \cos\left\{6N\Omega_D^I(\tau_R/2, 0)\right\} \\ & \times \sin\left\{6N\Omega_D^{II}(\tau_R/2 + t_1, t_1)\right\} \\ & \times \cos\left\{6N\Omega_D^I(\tau_R/2 + t_1, t_1)\right\}. \end{aligned} \qquad [36]$$

It is to be noted that the presence of the two dipolar phase terms in Eq. [35] implies a dependence of the observed rotor-encoded heteronuclear MQ MAS spinning-sideband patterns upon the two dipolar coupling constants as well as the relative orientation of the two internuclear vectors, which define the two dipolar PASs.

For the spin-pair case, it has been shown (Figs. 7 and 9) that the observed heteronuclear MQ MAS spinning-sideband patterns are sensitive to the relative orientation of the dipolar and quadrupolar PASs. On the basis of this observation, a complicated and intractable dependence on the many angles describing the relative orientations of three PASs is to be expected for an IS_2 system. However, simulations reveal that only the single angle defining the *relative orientation of the two IS internuclear vectors* has a marked effect on the appearance of the heteronuclear MQ MAS spinning-sideband pattern. This marked dependence is illustrated in Fig. 16a, which shows the change in the intensity (relative to that of the first-order sidebands) of the third- (squares), fifth- (crosses), and seventh- (triangles) order spinning-sidebands as a function of the H–Na–H angle for a heteronuclear MQ MAS experiment corresponding to that of Fig. 15c. In these simulations, both Na–H dipolar couplings are the same (1.6 kHz), and the *z* axis of the quadrupolar PAS is oriented such that it bisects the H–Na–H angle. In Fig. 17, the simulated spinning-sideband patterns corresponding to H–Na–H angles of (Fig. 17a) 170°, (17b) 174°, and (17c) 180° are presented. It is evident that the observed spinning-sideband intensities are particularly sensitive in the region corresponding to H–Na–H angles between 170° and 180°. The comparative insensitivity upon the orientation of the quadrupolar PAS with respect to the dipolar PASs is illustrated by Fig. 16b, which shows the effect of changing the orientation of the *z* axis of the quadrupolar PAS for a fixed H–Na–H angle equal to 170°. For the third- and fifth-order sidebands, the relative intensities vary within the ranges 31–35% and 20–25%, respectively, while a slightly more pronounced sensitivity is observed for the relative intensity of the seventh-order sidebands (5–18%).

In Section 8, it was shown that the observation of small asymmetric spinning sidebands in the MQ MAS spectrum of Na_2HPO_4 (Fig. 10a) is due to the ^{23}Na CSA; for the Na(2) site, a good fit to the experimental spectrum was found for $\delta = 2.8$ kHz. To investigate the effect of a ^{23}Na CSA upon the

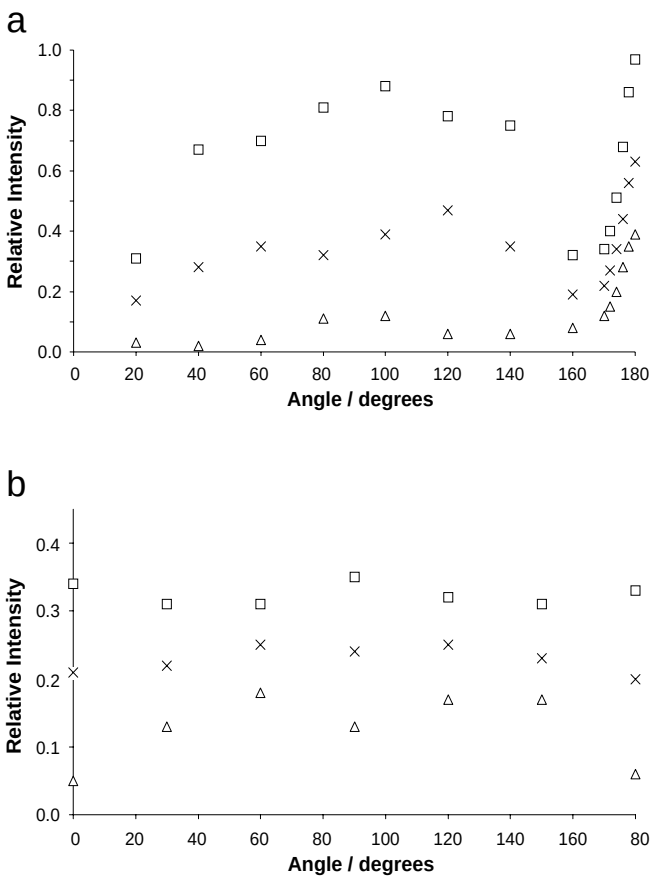

FIG. 16. The intensity of higher order odd spinning sidebands in spectra simulated for a three-spin (^{1}H ^{23}Na ^{1}H) system using the heteronuclear MQ MAS experiment in Fig. 1b as a function of (a) the H–Na–H angle and (b) the orientation of the z axis of the quadrupolar PAS with respect to one of the Na–H internuclear vectors. Relative intensities with respect to that of the first-order spinning sidebands are denoted by squares (third-order), crosses (fifth-order) and triangles (seventh-order). Density-matrix simulations were performed in the time domain using the SIMPSON (*67*) NMR simulation program. A representative SIMPSON input file is given in the Appendix. The following parameters were used: $C_Q = 1.4$ MHz; $\eta = 0.2$; $\nu_R = 10$ kHz; $\tau_{rcpl} = 3\ \tau_R$; ^{1}H 90° pulse length = 2.2 μs; ^{23}Na 90° pulse length = 1.5 μs; ^{23}Na pulse lengths for 3Q excitation, 3Q inversion, and 3Q to 1Q conversion = 3.6, 3.0, and 1.5 μs, respectively. For both Na–H spin pairs, $D_{IS}/2\pi = 1.6$ kHz. The homonuclear proton–proton dipolar coupling and ^{23}Na CSA were neglected. In (a), the z axis of the quadrupolar PAS is oriented such that it bisects the H–Na–H angle. In (b), the H–Na–H angle equals 170°.

appearance of heteronuclear MQ MAS spinning-sideband patterns, density matrix simulations including a ^{23}Na CSA were performed for the same spin system and experimental parameters as in Fig. 17a, i.e., the H–Na–H angle equals 170°, with the z axis of the quadrupolar PAS bisecting the H–Na–H angle. Figure 18 presents such simulated spectra for a ^{23}Na CSA of $\delta = 3.0$ kHz and $\eta = 0$, where the angle between the z axes of the CSA and quadrupolar PASs are (Fig. 18a) 0°, (18b) 45°, and (18c) 90°. For comparison, Fig. 18d presents the corresponding pattern for the case where the ^{23}Na CSA is neglected (repeated from Fig. 17a).

An inspection of Fig. 18 reveals that the ^{23}Na CSA is responsible for the introduction of a small asymmetry between positive and negative sidebands of the same order, with the effect being most pronounced for the first-order sidebands; such small asymmetries are observed in the experimental spectra in Fig. 15. It is to be noted that similar asymmetries due to CSA effects have been observed in ^{1}H–^{1}H DQ MAS spinning-sideband patterns (*19, 98*). Changing the relative orientation of the CSA and quadrupolar PASs leads to only small changes in the observed patterns. Further simulated spectra (not shown) indicate that the observed patterns are also similarly insensitive to the CSA asymmetry parameter; notably, as in the case of MQ

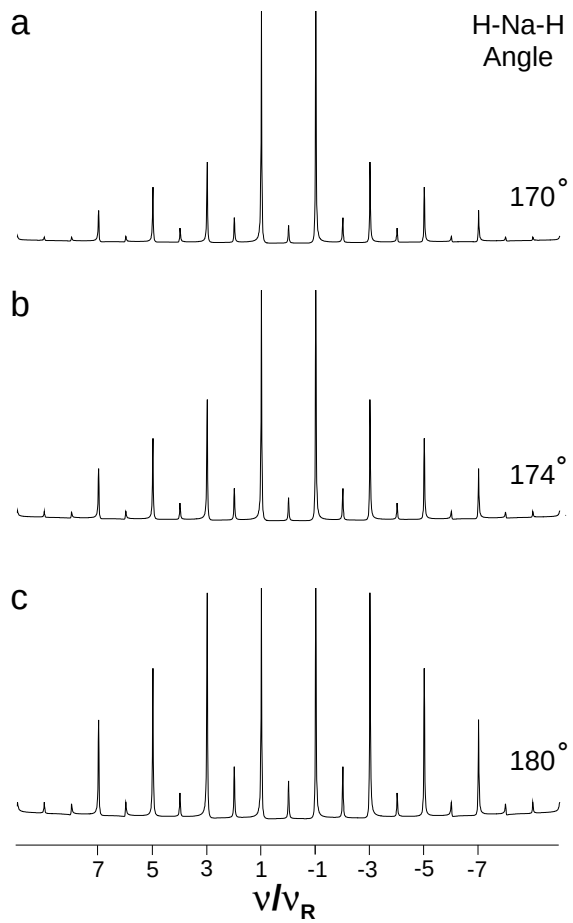

FIG. 17. Spinning-sideband patterns simulated for a three-spin system using the heteronuclear MQ MAS experiment in Fig. 1b, where the H–Na–H angle equals (a) 170°, (b) 174°, (c) 180°. Density-matrix simulations were performed in the time domain using the SIMPSON (*67*) NMR simulation program. A representative SIMPSON input file is given in the Appendix. The following parameters were used: $C_Q = 1.4$ MHz; $\eta = 0.2$; $\nu_R = 10$ kHz; $\tau_{rcpl} = 3\ \tau_R$; ^{1}H 90° pulse length = 2.2 μs; ^{23}Na 90° pulse length = 1.5 μs; ^{23}Na pulse lengths for 3Q excitation, 3Q inversion, and 3Q to 1Q conversion = 3.6, 3.0, and 1.5 μs, respectively. For both Na–H spin pairs, $D_{IS}/2\pi = 1.6$ kHz, while the z axis of the quadrupolar PAS is oriented at an angle of (a) 85°, (b) 87°, and (c) 90° with respect to the two dipolar PASs. The homonuclear proton–proton dipolar coupling and ^{23}Na CSA were neglected.

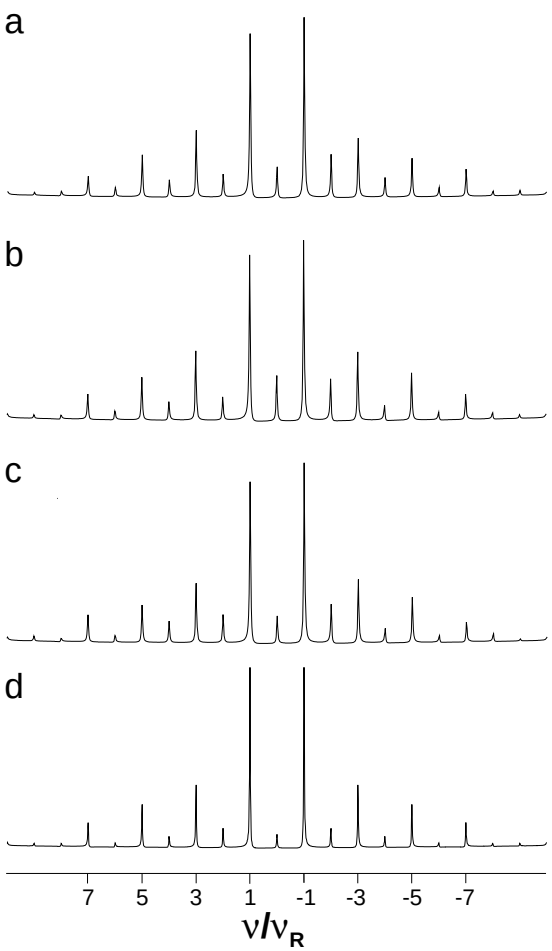

FIG. 18. Spinning-sideband patterns simulated for a three-spin (H–Na–H) system using the heteronuclear MQ MAS experiment in Fig. 1b, where (a)–(c) a ^{23}Na CSA of $\delta = 3.0$ kHz and $\eta = 0$ is considered. The angle between the z axes of the CSA and quadrupolar PASs equals (a) 0°, (b) 45°, and (c) 90°. In (d), the ^{23}Na CSA is neglected. Density-matrix simulations were performed in the time domain using the SIMPSON (*67*) NMR simulation program. A representative SIMPSON input file is given in the Appendix. The same parameters as in Fig. 17a were used.

MAS spinning-sideband patterns (see Section 8), the asymmetry remains for $\eta = 1$. Importantly, comparing the spectra in Figs. 18a–18c with that in Fig. 18d, it is apparent that the average (for the positive and negative sidebands) odd-order sideband intensities for the simulations including a ^{23}Na CSA are not significantly changed as compared to the case where the ^{23}Na CSA is neglected. Greater centerband and even-order sideband intensity is observed when the ^{23}Na CSA is considered.

Section 9 demonstrated that the evolution during t_1 of the ^{1}H transverse magnetization part of the mixed coherence state under homonuclear dipolar couplings to other protons leads to a rapid decay of the t_1 FID in the heteronuclear MQ MAS experiment. The question must then be asked, do homonuclear dipolar couplings affect the observed heteronuclear MQ MAS spinning-sideband patterns? To address this question, consider Fig. 19, which presents MQ spinning-sideband patterns obtained for Na_2HPO_4 using the heteronuclear (^{23}Na–^{1}H) MQ MAS (with a ^{1}H spinlock during t_1) pulse sequence in Fig. 1b, where the MAS frequency was 10 kHz in Fig. 19a and 20 kHz in Fig. 19b. Two and four rotor periods of recoupling were used in Fig. 19a and 19b, respectively, such that the total recoupling time was the same (200 μs) in both cases. Note that the apparent reduction in linewidth in Fig. 19b is largely a consequence of the doubling of the spectral width in this case.

It was shown in Section 9 that an increase in the MAS frequency leads to more efficient homonuclear dipolar decoupling. Thus, if homonuclear ^{1}H dipolar couplings significantly

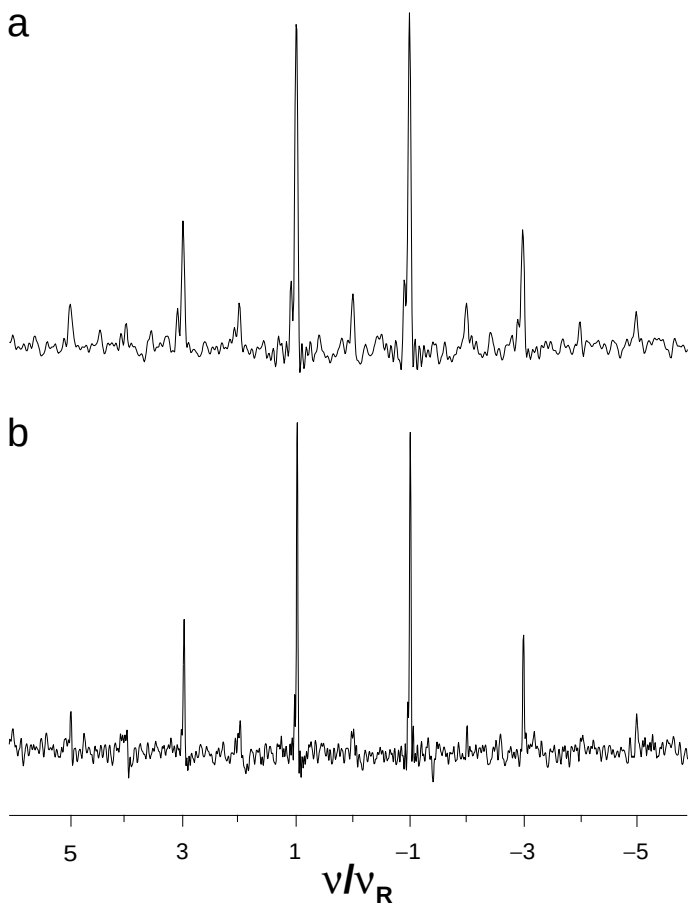

FIG. 19. MQ spinning-sideband patterns obtained for Na_2HPO_4 using the heteronuclear (^{23}Na–^{1}H) MQ MAS (with a ^{1}H spinlock during t_1) pulse sequence in Fig. 1b. The MAS frequency was 10 kHz in (a) and 20 kHz in (b). Two and four rotor periods of recoupling were used in (a) and (b), respectively, such that the total recoupling time was the same (200 μs) in both cases. The presented spectra correspond to a summation over the F_2 spectral range due to the Na(2) site for sheared two-dimensional spectra. Sign discrimination was restored in the F_1 dimension for the ^{23}Na resonances by the TPPI (*99*) method, which involves incrementing the phases of the ^{23}Na pulses applied before t_1 by 30° after recording each t_1 point. In (a) and (b), respectively, 288 and 144 transients were coadded for each of 370 and 740 t_1 points, with a t_1 increment of 3.5 and 1.75 μs and a recycle delay of 1.4 and 1.4 s.

affect the sideband patterns, marked differences should be apparent on doubling the MAS frequency. By contrast, if only a simple rotor-encoding of the heteronuclear dipolar coupling would be acting, identical sideband patterns would be obtained. Considering the dominant odd-order spinning sidebands, a close similarity between the two patterns in Fig. 19 is observed, while the centerband and even-order sideband intensity is reduced at the higher ν_R. The latter effect is, however, most likely a consequence of a reduction in sideband intensity due to the $t_1$evolution of ^{23}Na 3QC under the ^{23}Na CSA. It can, thus, be concluded that homonuclear dipolar couplings do not contribute significantly to the observed spinning-sideband patterns. This conclusion is not surprising since, first, homonuclear ^{1}H dipolar couplings are suppressed during t_1 by the application of a ^{1}H spin lock and, second, no transverse ^{1}H magnetization state is present during the two REDOR recoupling periods. Moreover, compared to a typical organic solid, there is not a dense dipolar-coupled ^{1}H network in Na_2HPO_4; according to the crystal structure presented in Ref. (*63*), the shortest ^{1}H–^{1}H distance is 0.34 nm.

On the basis of the above discussion, it has been identified, by means of density-matrix simulations, that, considering the free parameters, the appearance of heteronuclear MQ MAS spinning-sideband patterns for an IS_2 system is particularly sensitive to only, first, the angle between the two IS internuclear vectors and, second, the two heteronuclear dipolar couplings. It should, thus, be possible to determine these structural parameters by means of a comparison of the extracted experimental spinning-sideband intensity ratios in Table 4 with the values extracted from spectra simulated for different values of the H–Na–H angle and the two Na–H dipolar couplings.

According to the refined crystal structure presented in Ref. (*63*), for the Na(2) site, there are two equidistant (0.270 nm) protons, with the H–Na–H vector being linear (see Table 2). The heteronuclear MQ MAS spinning-sideband pattern in Fig. 17c was simulated using the crystal-structure arrangement. An inspection of the 3rd:1st and 5th:1st spinning-sideband intensity ratios reveals major discrepancies as compared to the experimental values in Table 4. It is, thus, concluded that the proton localization around the Na(2) site in the refined crystal

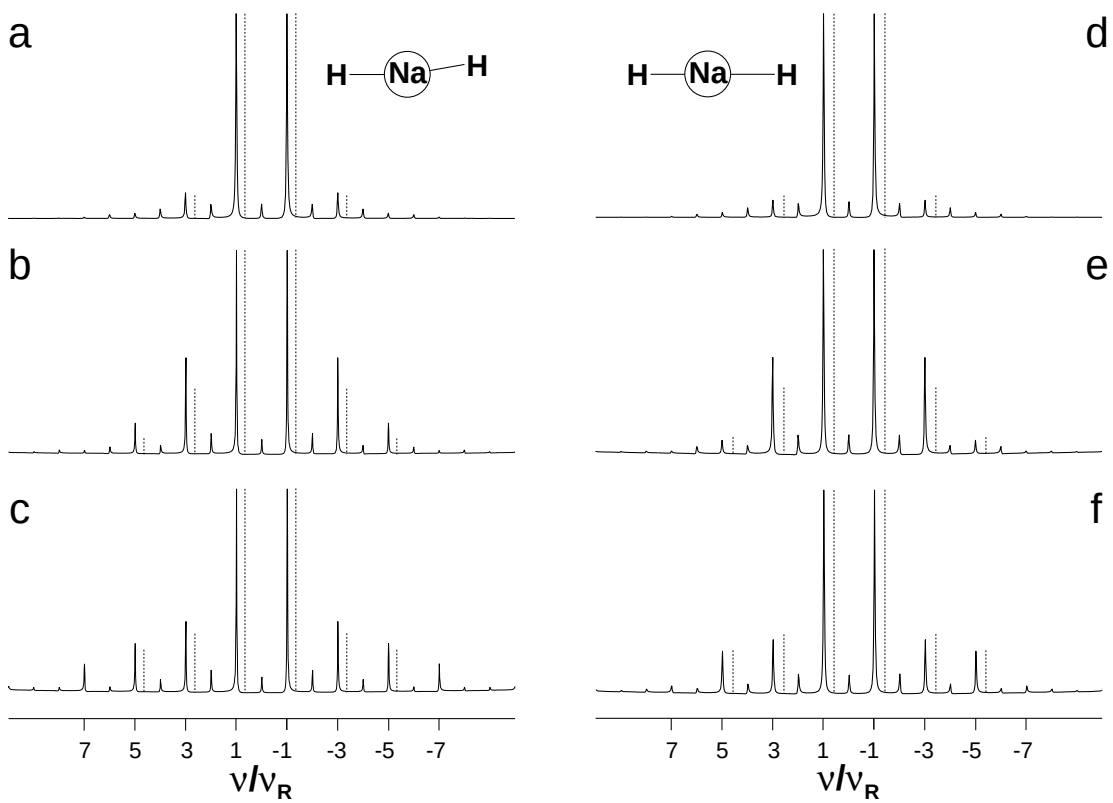

FIG. 20. A comparison of spinning-sideband patterns (solid lines) simulated for two distinct three-spin (H–Na–H) systems using the heteronuclear MQ MAS experiment in Fig. 1b with the extracted intensities (dashed lines) of the 1st-, 3rd-, and 5th-order spinning sidebands (see Table 4) for the experimental spectra in Fig. 15. The MAS frequency was 10 kHz, and the recoupling times were (a, d) one, (b, e) two, and (c, f) three rotor periods. In (a)–(c), the H–Na–H angle is 170° and the two Na–H distances are identical (0.266 nm, corresponding to $D_{IS}/2\pi = 1.6$ kHz), while in (d)–(f), the H–Na–H angle is 180°, and the two Na–H distances are different (0.266 and 0.311 nm, corresponding to $D_{IS}/2\pi = 1.6$ and 1.0 kHz, respectively). Density-matrix simulations were performed in the time domain using the SIMPSON (*67*) NMR simulation program. A representative SIMPSON input file is given in the Appendix. All other parameters are the same as in Fig. 17a.

structure of Na_2HPO_4 presented in Ref. (*63*) is erroneous. Instead, as demonstrated in Fig. 20, we found that good agreement with respect to the experimental data was achieved for two different structural arrangements, whereby either there is a deviation of 10° from linearity for the case of two identical Na–H distances (left-hand side of Fig. 20), or the linear arrangement is retained, but the two Na–H distances are different (right-hand side of Fig. 20). It is to be noted that the 7th:1st sideband ratio for the $\tau_{rcpl} = 3\ \tau_R$ patterns was not optimized, since it has been shown above that this ratio is additionally sensitive to the orientation of the quadrupolar PAS.

SUMMARY AND OUTLOOK

In this paper, a new heteronuclear MQ MAS experiment suitable for application to dipolar-coupled half-integer quadrupolar and spin $I = 1/2$ nuclei has been presented. The experiment involves the evolution of a heteronuclear MQC comprising 3QC of the half-integer quadrupolar nucleus and SQC coherence of the spin $I = 1/2$ nucleus. As far as the half-integer quadrupolar nucleus is concerned, the correlation of 3QC evolution during t_1 with SQC evolution during t_2 ensures, as demonstrated in Fig. 10b, that the well-known ability of the (homonuclear) MQ MAS experiment to yield high-resolution spectra due to the refocusing of the residual second-order quadrupolar broadening is retained. The creation of the heteronuclear MQC depends on the presence of a dipolar coupling between the half-integer quadrupolar nucleus and the spin $I = 1/2$ nucleus, with the REDOR pulse sequence being employed to recouple the heteronuclear dipolar coupling during an excitation and a reconversion period. Thus, signal is only observed for those quadrupolar nuclei having a close proximity to a spin $I = 1/2$ nucleus.

This paper has focused, in particular, on the spinning-sideband patterns which are observed in the indirect dimension of the heteronuclear MQ MAS experiment. It was shown analytically, for the case of an isolated spin pair, that the rotor encoding of the heteronuclear dipolar coupling alone leads to sideband patterns (see Fig. 5) where only odd-order sideband intensity is observed, with the nature of the pattern depending on the product of the dipolar coupling and the recoupling time. Considering realistic experimental conditions, density-matrix simulations (see Figs. 6–9) showed that the sideband patterns are also sensitive to the quadrupolar parameters (which can be determined from a homonuclear MQ MAS experiment) as well as, for an isolated spin pair, the relative orientation of the dipolar and quadrupolar PASs. Considering the various angles defining the orientations of the quadrupolar PAS and the two dipolar PASs in an IS_2 spin system, it was shown that the sideband patterns are particularly sensitive to only the angle between the two IS internuclear vectors (see Fig. 16).

The viability of the method was experimentally demonstrated using Na_2HPO_4. Specifically, heteronuclear MQ MAS spinning-sideband patterns obtained for the Na(2) site were analysed. A crystal structure (*63*) is available for Na_2HPO_4 which indicates that there are two protons equidistant to the Na(2) nucleus. In spite of the complications caused by the need to consider the three spin H–Na–H system, it proved possible to derive valuable structural information from an analysis of the experimental heteronuclear MQ MAS sideband patterns (see Fig. 15). It was demonstrated that the proton localization around the Na(2) site according to the literature crystal structure of Na_2HPO_4 is erroneous. Instead, the experimental data was found to be consistent with two alternative different structural arrangements, whereby either there is a deviation of 10° from linearity for the case of two identical Na–H distances, or there is a linear arrangement, but the two Na–H distances are different. In addition, it was shown in Section 8 that the asymmetry in the experimental (homonuclear) MQ MAS sideband pattern for the Na(2) site, where the second-order quadrupolar broadening is small, can only be explained by a consideration of the ^{23}Na CSA.

In a previous study, we and other co-workers have presented MQ MAS spinning-sideband patterns for spin $I = 3/2$ (^{23}Na) and 5/2 (^{27}Al) nuclei (*53*) in samples where there is a single distinct nuclear site for which the C_Q value is small. In particular, for the aluminum sample, experiments whereby ^1H dipolar decoupling was achieved by either partial deuteration or by the application of *rf* pulses allowed an investigation of the contribution of the Al–H heteronuclear dipolar coupling to the observed sideband pattern. It was shown that the effect was, as is also the case in the work presented in this paper, magnified in the MQ as compared to the SQ experiment. It should be noted that this previous study differs from the study described in this paper in that spinning-sideband patterns corresponding to the break-up of the whole first-order quadrupolar-broadened static spectrum were observed. In addition, a simple two-pulse sequence, where the evolution period between the two pulses is restricted to a duration of $\tau_R/2$, was used for the excitation and reconversion of MQC.

Various modifications of the pulse sequence presented here can be envisaged. Of particular interest would be the incorporation of whole-echo acquisition (*72*, *75*), which would involve the selection of either $+3$ or -3 coherence for the half-integer quadrupolar nucleus during t_1. Such an approach would offer the following advantages: first, a more efficient 3QC to SQC conversion would be possible by means of the use of a DFS (*76*) or FAM (*77*) pulse; second, the experiment is inherently sign sensitive with regards to the half-integer quadrupolar nucleus, such that a TPPI (*99*) approach or similar could be used to achieve sign discrimination in t_1 for the spin $I = 1/2$ nucleus. The latter advantage would be of particular importance for the case where more than one distinct spin $I = 1/2$ nuclei have close proximities to the half-integer quadrupolar nuclei. In such a case, it would be informative to perform a rotor-synchronized (the t_1 increment is set equal to τ_R) experiment (*15, 100*), in which all the spinning sidebands can be considered to fold in at the centerband position. It is to be noted that the application of a ^1H spin lock during t_1 would result in a loss of ^1H chemical

shift information, and instead either very-fast MAS or a homonuclear proton decoupling scheme would have to be employed. In addition to improving the sensitivity of the 3QC to SQC step, it is to be expected that an improved method could be found for inverting the half-integer quadrupolar nucleus MQC. Finally, the experiment can, of course, be applied to other half-integer quadrupolar nuclei, e.g., spin $I = 5/2$ nuclei such as ^{17}O and ^{27}Al (for which 5Q as well as 3Q experiments would be possible), as well as to other spin $I = 1/2$ nuclei, e.g., ^{31}P.

APPENDIX

Derivation of Eq. [16]

For the quadrupolar Hamiltonian for a single spin, $[H(t_a), H(t_b)] = 0$, and the Dyson time-ordering operator can hence be dropped from Eq. [14], i.e.,

$$U(t_b, t_a) = \exp\left\{-i \int_{t_a}^{t_b} H(t)\, dt\right\}. \quad [A1]$$

Using the identity $\sum_a |a\rangle\langle a| = 1$, (*101*), the following expression is valid for any operator and any basis {a}:

$$U = \sum_{a,b} |a\rangle\langle a|U|b\rangle\langle b|. \quad [A2]$$

The quadrupolar Hamiltonian, $H_Q(t)$, is diagonal in the Zeeman basis. Thus, if $|m\rangle$ is a Zeeman eigenstate

$$H_Q(t)|m\rangle = e_m(t)|m\rangle, \quad [A3]$$

where

$$e_m(t) = \langle m|H_Q(t)|m\rangle. \quad [A4]$$

Any operator which is a function of another operator has eigenvalues corresponding to the operation of this function on the eigenvalues of the latter operator, i.e., if

$$H(t)|m\rangle = e_m(t)|m\rangle, \quad [A5]$$

then

$$f(H(t))|m\rangle = f(e_m(t))|m\rangle. \quad [A6]$$

Therefore,

$$\exp\left\{\int_{t_a}^{t_b} H_Q(t)\, dt\right\}|m\rangle = \exp\left\{\int_{t_a}^{t_b} e_m(t)\, dt\right\}|m\rangle. \quad [A7]$$

Using the orthogonality of the Zeeman eigenfunctions, i.e., $\langle n||m\rangle = \delta_{nm}$, where the Kronecker delta, δ_{nm}, is equal to one if $n = m$ and zero otherwise, the following is obtained

$$\langle n|\exp\left\{\int_{t_a}^{t_b} H(t)\, dt\right\}|m\rangle = \exp\left\{\int_{t_a}^{t_b} e_m(t)\, dt\right\}\delta_{nm}. \quad [A8]$$

Using Eqs. [A2], [A4], and [A8], Eq. [A1] is transformed into Eq. [16]:

$$U_Q(t_b, t_a) = \sum |m_I\rangle\langle m_I|\exp\left\{-i\int_{t_a}^{t_b}\langle m_I|H_Q(t)|m_I\rangle\, dt\right\}. \quad [A9]$$

Derivation of Eq. [34]

From Section 4,

$$S_D(t_1) = \sin\left\{\frac{6\sqrt{2}ND_{IS}}{\omega_R}\sin(2\theta)\sin(\varphi)\right\} \times \sin\left\{\frac{6\sqrt{2}ND_{IS}}{\omega_R}\sin(2\theta)\sin(\omega_R t_1 + \varphi)\right\}. \quad [B1]$$

The $\sin\{\alpha \sin\beta\}$ terms in Eq. [B1] can be expanded as sums of Bessel functions (*102*):

$$\sin\{\alpha\sin\beta\} = 2\sum_{n=0}^{+\infty} J_{2n+1}(\alpha)\sin\{(2n+1)\beta\}. \quad [B2]$$

Equation [B1], thus, becomes

$$\begin{aligned} S_D(t_1) &= 4\sum_{m=0}^{+\infty}\sum_{n=0}^{+\infty} J_{2m+1}\left(\frac{6\sqrt{2}D_{IS}N\tau_R}{2\pi}\sin(2\theta)\right) \\ &\quad \times J_{2n+1}\left(\frac{6\sqrt{2}D_{IS}N\tau_R}{2\pi}\sin(2\theta)\right)\sin\{(2m+1)\varphi\} \\ &\quad \times \sin\{(2n+1)(\omega_R t_1 + \varphi)\} \\ &= 4\sum_{m=0}^{+\infty}\sum_{n=0}^{+\infty} J_{2m+1}\left(\frac{6\sqrt{2}D_{IS}N\tau_R}{2\pi}\sin(2\theta)\right) \\ &\quad \times J_{2n+1}\left(\frac{6\sqrt{2}D_{IS}N\tau_R}{2\pi}\sin(2\theta)\right)\sin\{(2m+1)\varphi\} \\ &\quad \times [\sin\{(2n+1)\omega_R t_1\}\cos\{(2n+1)\varphi\} \\ &\quad + \cos\{(2n+1)\omega_R t_1\}\sin\{(2n+1)\varphi\}]. \end{aligned} \quad [B3]$$

Equation [34] is, hence, derived by taking the powder average

over the angle φ

$$\langle S_D(t_1)\rangle_\varphi = \frac{1}{2\pi}\int_0^{2\pi} S_D(t_1)\,d\varphi$$
$$= 2\sum_{n=0}^{+\infty}\left\{J_{2n+1}\left(\frac{6\sqrt{2}D_{IS}N\tau_R}{2\pi}\sin(2\theta)\right)\right\}^2 \times \cos\{(2n+1)\omega_R t_1\}, \quad [B4]$$

where use is made of the following relations:

$$\int_0^{2\pi}\sin(A\varphi)\sin(B\varphi)\,d\varphi = \pi \quad \text{if A} = \text{B} \quad [B5]$$

$$\int_0^{2\pi}\sin(A\varphi)\sin(B\varphi)\,d\varphi = 0 \quad \text{if A} \neq \text{B} \quad [B6]$$

$$\int_0^{2\pi}\cos(A\varphi)\sin(B\varphi)\,d\varphi = 0 \quad \text{for all cases.} \quad [B7]$$

Representative SIMPSON Input Files

The following points should be noted:

(i) Only a t_1 FID is simulated (solely the first point in t_2 is acquired).
(ii) Second-order quadrupolar effects are not considered.
(iii) Only the $p = -3$ pathway is selected during t_1, such that sign discrimination is ensured.

The Heteronuclear MQ MAS Experiment

The following input file corresponds to the case of an isolated spin pair.

```
spinsys {
   channels    23Na 1H
   nuclei      23Na 1H
   quadrupole  1 1 1.e6 0. 0 0 0
   dipole      1 2 −2500 0 90 0
}
par {
   conjugate_fid  false
   spin_rate      10000
   variable Trot  1.e6/spin_rate
   variable Nrot  3
   variable n     20
   sw             spin_rate*n
   crystal_file   rep256
   gamma_angles   19
   np             n
   start_operator    I1z
   detect_operator   I1c
   verbose           1101
   proton_frequency  500e6
   variable tsw      1.0e6/sw
   variable tau2     1.5
   variable tau1     2.4*tau2
   variable tinv     2*tau2
   variable rf       1.e6/tau2/4
   variable p90      2
   variable p180     2*p90
   variable rfH      1.e6/p90/4
   variable d        Trot/2-p180
}
proc pulseq {} {
   global par t
   matrix set 1 coherence {{3 1}{3 −1}}
   matrix set 2 coherence {{−3 1}{−3 −1}}
   maxdt 0.5
#  CALCULATE PROPAGATORS FOR
   RECONVERSION (AFTER t1)
     for {set i 1} {$i <= $par(n)} {incr i} {
      maxdt 1

     reset [expr
$par(tau1)+$par(Nrot)*$par(Trot)+1*$par
  (tinv)+$par(p90)+($i−1)*$par(tsw)]

     pulse $par(p90) 0 0 $par(rfH) 270
     delay $par(d)
     pulse $par(p180) 0 0 $par(rfH) 0
     delay $par(d)
     pulse $par(p180) 0 0 $par(rfH) 180
     delay $par(d)
     pulse $par(p180) 0 0 $par(rfH) 0
     delay $par(d)
     pulse $par(p180) 0 0 $par(rfH) 180
     delay $par(d)
     pulse $par(p180) 0 0 $par(rfH) 0
     delay $par(d)
     pulse $par(p180) 0 0 $par(rfH) 180
     maxdt 0.5

     pulse $par(tau2) $par(rf) 270 0 0
     store $i
}
#  CALCULATE PROPAGATORS FOR 3Q
     EXCITATION (P1), 3Q INVERSION (P3)
#  AND THE FIRST REDOR RECOUPLING PERIOD
    AND FIRST 1H PI/2 PULSE (P2)
   reset
      set p1 [expr 2*$par(n) + 1]
      set p2 [expr 2*$par(n) + 2]
```

```
      set p3 [expr 2*$par(n) + 3]
      maxdt 0.5
      pulse $par(tau1) $par(rf) 0 0 0
      store $p1
      reset [expr $par(tau1)]
      maxdt 1

      delay $par(d)
      pulse $par(p180) 0 0 $par(rfH) 0
      delay $par(d)
      pulse $par(p180) 0 0 $par(rfH) 180

      delay $par(d)
      pulse $par(p180) 0 0 $par(rfH) 0
      delay $par(d)
      pulse $par(p180) 0 0 $par(rfH) 180

      delay $par(d)
      pulse $par(p180) 0 0 $par(rfH) 0
      delay $par(d)
      pulse $par(p180) 0 0 $par(rfH) 180

      pulse $par(p90) 0 0 $par(rfH) 90
      store $p2
      reset [expr $par(tau1)+$par(Nrot)
      *$par(Trot)+$par(p90)]
      maxdt 0.5
      pulse $par(tinv) $par(rf) 90 0 0
      store $p3

#  THE ACTUAL PULSE SEQUENCE
   for {set i 1} {$i <= $par(np)} {incr i} {
     set t1 [expr ($i-1)*$par(tsw)]
     reset
     prop $p1
     prop $p2
     filter 1
     prop $p3
     filter 2
     maxdt 10
     turnoff all
     delay $t1
     turnon all
     prop [expr ($i-1) % $par(n) + 1]
     acq
}

}
proc main {} {
   global par
   set f [fsimpson]
   fsave $f $par(name).fid
   funload $f
}
```

The simulations for the three-spin system used the same basic program, with it only being necessary to change the spin system and filter definitions to:

```
spinsys {
   channels    23Na 1H
   nuclei      23Na 1H 1H
   quadrupole  1 1 1.38e6 0.2 0 85 0
   dipole      1 2 -1600 0 0 0
   dipole      1 3 -1600 0 170 0
}

    matrix set 1 coherence {{3 1 0}
    {3 -1 0} {3 0 1} {3 0 -1}}
    matrix set 2 coherence {{-3 1 0}
    {-3 -1 0} {-3 0 1} {-3 0 -1}}
```

It is to be noted that all interactions are "turned off" during t_1. In this way, the action of the ^{1}H spin lock in suppressing evolution under the second heteronuclear dipolar coupling is taken into account. (Note that there is no evolution of 3QC under a first-order quadrupolar coupling.)

In simulations including the ^{23}Na CSA, the following line was added to the spin system part:

```
shift 1 0 3000 0.5 0 130 0
```

In addition, to observe the evolution under the CSA during t_1, the relevant lines of the pulse sequence part was changed to

```
turnoff quadrupole_1 dipole_1_2 dipole_1_3
delay $t1
turnon quadrupole_1 dipole_1_2 dipole_1_3
```

The (Homonuclear) MQ MAS Experiment

```
spinsys {
   channels 23Na
   nuclei 23Na
   quadrupole 1 1 1.38e6 0.2 0 0 0
   shift 1 0 3000 0. 0 90 0
}
par {
   spin_rate          10000
   variable n         10
   sw                 spin_rate*n
   crystal_file       rep256
   gamma_angles       21
   np                 n
   start_operator     I1z
   detect_operator    I1c
   verbose            1101
   proton_frequency   500e6
   variable nprim     np
   variable tsw       1.e6/sw
   variable tau2      1.75
   variable tau1      3.5
   variable rf        1.e6/tau2/4
}
```

```
proc pulseq {} {
   global par t
   matrix set 1 coherence {{-3}}
   maxdt 0.5

   for {set i 1} {$i <= $par(n)} {incr i} {
     reset [expr $par(tau1)+($i-1)
     *$par(tsw)]
     pulse $par(tau2) $par(rf) 90
     store $i
}
   reset
   set p1 [expr 2*$par(n) + 1]
   pulse $par(tau1) $par(rf) 0
   store $p1

   for {set i 1} {$i <= $par(np)} {incr i} {
     set t1 [expr ($i-1)*$par(tsw)]
     reset
     prop $p1
     filter 1
     maxdt 2
     delay $t1
     prop [expr ($i-1) % $par(n) + 1]
     acq 90
}
}
proc main {} {
   global par
   set f [fsimpson]
   fsave $f $par(name).fid
   funload $f
}
```

ACKNOWLEDGMENTS

A. L. thanks the DAAD for the award of a Jahresstipendium. Stimulating discussions with Sharon Ashbrook, Ingo Schnell, Kay Saalwächter, and Stephen Wimperis are acknowledged. We thank Stefan Steuernagel for technical advice concerning the implementation of the frequency-domain shearing transformation.

REFERENCES

1. K. Schmidt-Rohr and H. W. Spiess, "Multidimensional Solid-State NMR and Polymers," Academic Press, London (1994).
2. M. E. Smith and E. R. H. van Eck, *Prog. NMR Spectrosc*. **34,** 159 (1999).
3. A. J. Vega, *in* "Encyclopedia of Nuclear Magnetic Resonance" (D. M. Grant and R. K. Harris, Eds.), Vol. 6, p. 3869, Wiley, Chichester (1996).
4. S. Ganapathy, S. Schramm, and E. Oldfield, *J. Chem. Phys.* **77,** 4360 (1982).
5. L. Frydman and J. S. Harwood, *J. Am. Chem. Soc.* **117,** 5367 (1995).
6. S. P. Brown and S. Wimperis, *J. Magn. Reson.* **128,** 42 (1997).
7. T. Vosegaard, P. Florian, P. J. Grandinetti, and D. Massiot, *J. Magn. Reson.* **143,** 217 (2000).
8. M. Pruski, J. W. Wiench, and J.-P. Amoureux, *J. Magn. Reson.* **147,** 286 (2000).
9. J. Rocha, A. P. Esculas, C. Fernandez, and J. P. Amoureux, *J. Phys. Chem.* **100,** 17889 (1996).
10. P. J. Dirken, S. C. Kohn, M. E. Smith, and E. R. H. van Eck, *Chem. Phys. Lett.* **266,** 568 (1997).
11. Z. Xu, H. Maekawa, J. V. Oglesby, and J. F. Stebbins, *J. Am. Chem. Soc.* **120,** 9894 (1998).
12. S. P. Brown, S. E. Ashbrook, and S. Wimperis, *J. Phys. Chem. B* **103,** 812 (1999).
13. S. Caldarelli and F. Ziarelli, *J. Am. Chem. Soc.* **122,** 12015 (2000).
14. L. B. Alemany, R. L. Callender, A. R. Barron, S. Steuernagel, D. Iuga, and A. P. M. Kentgens, *J. Phys. Chem. B* **104,** 11612 (2000).
15. I. Schnell, S. P. Brown, H. Y. Low, H. Ishida, and H. W. Spiess, *J. Am. Chem. Soc.* **120,** 11784 (1998).
16. S. P. Brown, I. Schnell, J. D. Brand, K. Müllen, and H. W. Spiess, *J. Am. Chem. Soc.* **121,** 6712 (1999).
17. L. N. J. Rodriguez, S. M. De Paul, C. J. Barrett, L. Reven, and H. W. Spiess, *Adv. Mater.* **12,** 1934 (2000).
18. S. P. Brown, T. Schaller, U. P. Seelbach, F. Koziol, C. Ochsenfeld, F.-G. Klärner, and H. W. Spiess, *Angew. Chem. Int. Ed. Engl.* **40,** 717 (2001).
19. S. P. Brown, X. X. Zhu, K. Saalwächter, and H. W. Spiess, *J. Am. Chem. Soc.* **123,** 4275 (2001).
20. Y. Ishii and R. Tycko, *J. Magn. Reson.* **142,** 199 (2000).
21. K. Yamauchi, S. Kuroki, K. Fujii, and I. Ando, *Chem. Phys. Lett.* **324,** 435 (2000).
22. H. Geen, J. J. Titman, J. Gottwald, and H. W. Spiess, *Chem. Phys. Lett.* **227,** 79 (1994).
23. B.-J. Van Rossum, H. Förster, and H. J. M. de Groot, *J. Magn. Reson.* **124,** 516 (1997).
24. A. Lesage, D. Sakellariou, S. Steuernagel, and L. Emsley, *J. Am. Chem. Soc.* **120,** 13,194 (1998).
25. A. Lesage, P. Charmont, S. Steuernagel, and L. Emsley, *J. Am. Chem. Soc.* **122,** 9739 (2000).
26. A. Lesage and L. Emsley, *J. Magn. Reson.* **148,** 449 (2001).
27. K. Saalwächter, R. Graf, and H. W. Spiess, *J. Magn. Reson.* **140,** 471 (1999).
28. K. Saalwächter, R. Graf, and H. W. Spiess, *J. Magn. Reson.* **148,** 398 (2001).
29. K. Saalwächter and H. W. Spiess, *J. Chem. Phys.* **114,** 5707 (2001).
30. A. Bielecki, A. C. Kolbert, and M. H. Levitt, *Chem. Phys. Lett.* **155,** 341 (1989).
31. T. Gullion and J. Schaefer, *Adv. Magn. Reson.* **13,** 57 (1989).
32. B.-J. van Rossum, C. P. de Groot, V. Ladizhansky, S. Vega, and H. J. M. de Groot, *J. Am. Chem. Soc.* **122,** 3465 (2000).
33. A. Fechtenkötter, K. Saalwächter, M. A. Harbison, K. Müllen, and H. W. Spiess, *Angew. Chem. Int. Ed. Engl.* **38,** 3039 (1999).
34. M. Hohwy, C. P. Jaroniec, B. Reif, C. M. Rienstra, and R. G. Griffin, *J. Am. Chem. Soc.* **122,** 3218 (2000).
35. D. McElheny, E. DeVita, and L. Frydman, *J. Magn. Reson.* **143,** 321 (2000).
36. G. R. Goward, I. Schnell, S. P. Brown, H. W. Spiess, H.-D. Kim, and H. Ishida, *Magn. Res. Chem.* **39,** S 5 (2001).
37. I. Schnell, B. Langer, S. H. M. Söntjens, M. H. P. van Genderen, R. P. Sijbesma, and H. W. Spiess, *J. Magn. Reson.* **150,** 57 (2001).
38. M. Pruski, D. P. Lang, C. Fernandez, and J. P. Amoureux, *Solid State Nucl. Magn. Reson.* **7,** 327 (1997).
39. C. Fernandez, L. Delevoye, J.-P. Amoureux, D. P. Lang, and M. Pruski, *J. Am. Chem. Soc.* **119,** 6858 (1997).

40. S. E. Ashbrook, S. P. Brown, and S. Wimperis, *Chem. Phys. Lett.* **288,** 509 (1998).
41. K. H. Lim and C. P. Grey, *Chem. Phys. Lett.* **312,** 45 (1999).
42. K. H. Lim and C. P. Grey, *J. Chem. Phys.* **112,** 7490 (2000).
43. D. Roynyak, M. Baldus, and R. G. Griffin, *J. Magn. Reson.* **142,** 145 (2000).
44. S. E. Ashbrook and S. Wimperis, *Mol. Phys.* **98,** 1 (2000).
45. S. E. Ashbrook, J. McManus, K. J. D. MacKenzie, and S. Wimperis, *J. Phys. Chem B* **104,** 6408 (2000).
46. S. E. Ashbrook and S. Wimperis, *J. Magn. Reson.* **147,** 238 (2000).
47. S. H. Wang, S. M. De Paul, and L. M. Bull, *J. Magn. Reson.* **125,** 364 (1997).
48. C. Fernandez, D. P. Lang, J. P. Amoureux, and M. Pruski, *J. Am. Chem. Soc.* **120,** 2672 (1998).
49. M. Pruski, A. Bailly, D. P. Lang, J.-P. Amoureux, and C. Fernandez, *Chem. Phys. Lett.* **307,** 35 (1999).
50. M. J. Duer and A. J. Painter, *Chem. Phys. Lett.* **313,** 763 (1999).
51. H. Geen, J. J. Titman, J. Gottwald, and H. W. Spiess, *J. Magn. Reson. A* **114,** 264 (1995).
52. J. Gottwald, D. E. Demco, R. Graf, and H. W. Spiess, *Chem. Phys. Lett.* **243,** 314 (1995).
53. U. Friedrich, I. Schnell, S. P. Brown, A. Lupulescu, D. E. Demco, and H. W. Spiess, *Mol. Phys.* **95,** 1209 (1998).
54. D. M. Gregory, M. A. Mehta, J. C. Shiels, and G. P. Drobny, *J. Chem. Phys.* **107,** 28 (1997).
55. A. Samoson, E. Kundla, and E. Lippmaa, *J. Magn. Reson.* **49,** 350 (1982).
56. P. P. Man, *in* "Encyclopedia of Nuclear Magnetic Resonance" (D. M. Grant and R. K. Harris, Eds.), Vol. 6, p. 3838, Wiley, Chichester (1996).
57. U. Haeberlen, "Advances in Magnetic Resonance" Suppl. 1, Academic Press, San Diego (1976).
58. R. N. Zare, "Angular Momentum," Wiley, Chichester (1988).
59. G. Wu and R. E. Wasylishen, *Mol. Phys.* **95,** 1177 (1998).
60. J. McManus, R. Kemp-Harper, and S. Wimperis, *Chem. Phys. Lett.* **311,** 292 (1999).
61. G. Wu and K. Yamada, *Chem. Phys. Lett.* **313,** 519 (1999).
62. S. Wi and L. Frydman, *J. Chem. Phys.* **112,** 3248 (2000).
63. M. Baldus, B. H. Meier, R. R. Ernst, A. P. M. Kentgens, H. Meyer zu Altenschildesche, and R. Nesper, *J. Am. Chem. Soc.* **117,** 5141 (1995).
64. A. Medek, J. S. Harwood, and L. Frydman, *J. Am. Chem. Soc.* **117,** 12,779 (1995).
65. J.-P. Amoureux, C. Fernandez, and L. Frydman, *Chem. Phys. Lett.* **259,** 347 (1996).
66. M. Feike, D. E. Demco, R. Graf, J. Gottwald, S. Hafner, and H. W. Spiess, *J. Magn. Reson. A* **122,** 214 (1996).
67. M. Baks, J. T. Rasmussen, and N. C. Nielsen, *J. Magn. Reson.* **147,** 296 (2000).
68. G. Bodenhausen, H. Kogler, and R. R. Ernst, *J. Magn. Reson.* **58,** 370 (1984).
69. P. J. Hore, J. A. Jones, and S. Wimperis, "NMR: The Toolkit," Chap. 6, Oxford University Press, Oxford (2000).
70. C. Fernandez and J. P. Amoureux, *Solid State Nucl. Magn. Reson.* **5,** 315 (1996).
71. C. Fernandez and J. P. Amoureux, *Chem. Phys. Lett.* **242,** 449 (1995).
72. D. Massiot, B. Touzo, D. Trumeau, J. P. Coutures, J. Virlet, P. Florian, and P. J. Grandinetti, *Solid State Nucl. Magn. Reson.* **6,** 73 (1996).
73. S. P. Brown, S. J. Heyes, and S. Wimperis, *J. Magn. Reson. A* **119,** 280 (1996).
74. J.-P. Amoureux, C. Fernandez, and S. Steuernagel, *J. Magn. Reson. A* **123,** 116 (1996).
75. S. P. Brown and S. Wimperis, *J. Magn. Reson.* **124,** 279 (1997).
76. A. P. M. Kentgens and R. Verhagen, *Chem. Phys. Lett.* **300,** 435 (1999).
77. P. K. Madhu, A. Goldbourt, L. Frydman, and S. Vega, *Chem. Phys. Lett.* **307,** 41 (1999).
78. G. Wu, D. Rovnyak, B. Sun, and R. G. Griffin, *Chem. Phys. Lett.* **249,** 210 (1996).
79. A. Wokaun and R. R. Ernst, *J. Chem. Phys.* **67,** 1752 (1977).
80. S. Vega and Y. Naor, *J. Chem. Phys.* **75,** 75 (1981).
81. J. Baum, M. Munowitz, A. N. Garroway, and A. Pines, *J. Chem. Phys.* **83,** 2015 (1985).
82. D. N. Shykind, J. Baum, S.-B. Liu, and A. Pines, *J. Magn. Reson.* **76,** 149 (1988).
83. H. Geen, R. Graf, A. S. D. Heindrichs, B. S. Hickman, I. Schnell, H. W. Spiess, and J. J. Titman, *J. Magn. Reson.* **138,** 167 (1999).
84. J.-P. Amoureux, M. Pruski, D. P. Lang, and C. Fernandez, *J. Magn. Reson.* **131,** 170 (1998).
85. T. Vosegaard, P. Florian, D. Massiot, and P. J. Grandinetti, *J. Chem. Phys.* **114,** 4618 (2001).
86. J. C. C. Chan and H. Eckert, *J. Magn. Reson.* **147,** 170 (2000).
87. T. Gullion and J. Schaefer, *J. Magn. Reson.* **92,** 439 (1991).
88. L. Marinelli and L. Frydman, *Chem. Phys. Lett.* **275,** 188 (1997).
89. T. Charpentier, C. Fermon, and J. Virlet, *J. Chem. Phys.* **109,** 3116 (1998).
90. M. J. Duer, *Chem. Phys. Lett.* **277,** 167 (1997).
91. S. H. Wang, Z. Xu, J. H. Baltisberger, L. M. Bull, J. F. Stebbins, and A. Pines, *Solid State Nucl. Magn. Reson.* **8,** 1 (1997).
92. A. Wong and G. Wu, *J. Phys. Chem. A* **104,** 11844 (2000).
93. E. D. Ostroff and J. S. Waugh, *Phys. Rev. Lett.* **16,** 1097 (1966).
94. M. Lee and W. I. Goldburg, *Phys. Rev. A* **140,** 1261 (1965).
95. A. Bielecki, A. C. Kolbert, H. S. M. de Groot, R. G. Griffin, and M. H. Levitt, *Adv. Magn. Reson.* **14,** 111 (1990).
96. E. Vinogradov, P. K. Madhu, and S. Vega, *Chem. Phys. Lett.* **314,** 443 (1999).
97. D. Sakellariou, A. Lesage, P. Hodgkinson, and L. Emsley, *Chem. Phys. Lett.* **319,** 253 (2000).
98. P. Tekeley, D. E. Demco, D. Canet, C. Malveau, *Chem. Phys. Lett.* **309,** 101 (1999).
99. D. Marion and K. Wüthrich, *Biochem. Biophys. Res. Commun.* **113,** 967 (1983).
100. D. Massiot, *J. Magn. Reson. A* **122,** 240 (1996).
101. P. W. Atkins, "Molecular Quantum Mechanics," 2nd ed., Oxford University Press, Oxford (1983).
102. M. Abramowitz and I. A. Stegun, "Handbook of Mathematical Functions," Dover, New York (1989).